



Published in final edited form as:

Nature. 2021 June ; 594(7863): 398–402. doi:10.1038/s41586-021-03552-w.

Interpreting type 1 diabetes risk with genetics and single cell epigenomics

Joshua Chiou^{1, #}, Ryan J Geusz¹, Mei-Lin Okino², Jee Yun Han³, Michael Miller³, Rebecca Melton¹, Elisha Beebe², Paola Benaglio², Serina Huang², Katha Korgaonkar², Sandra Heller⁴, Alexander Kleger⁴, Sebastian Preissl³, David U Gorkin^{3,5}, Maike Sander^{2,6,7}, Kyle J Gaulton^{2,7, #}

¹Biomedical Sciences Graduate Program, University of California San Diego, La Jolla CA 92093

²Department of Pediatrics, Pediatric Diabetes Research Center, University of California San Diego, La Jolla CA 92093

³Center for Epigenomics, Department of Cellular and Molecular Medicine, University of California San Diego, La Jolla CA 92093

⁴Department of Internal Medicine I, Ulm University, Ulm, Germany

⁵Current Address: Department of Biology, Emory University, Atlanta, GA 30322

⁶Department of Cellular and Molecular Medicine, University of California San Diego, La Jolla CA 92093

⁷Institute for Genomic Medicine, University of California San Diego, La Jolla CA 92093

SUMMARY

Genetic risk variants identified in genome-wide association studies (GWAS) of complex disease are primarily non-coding¹, and translating risk variants into mechanistic insight requires detailed gene regulatory maps in disease-relevant cell types². Here, we combined a GWAS of type 1 diabetes (T1D) in 520,580 samples with candidate *cis*-regulatory elements (cCREs) in pancreas

Reprints and permissions information is available at www.nature.com/reprints.

[#]Corresponding authors: Kyle J Gaulton, 9500 Gilman Drive, #0746, Department of Pediatrics, University of California San Diego, 858-822-3640, kgaulton@ucsd.edu, Joshua Chiou, 9500 Gilman Drive, #0746, Biomedical Sciences Graduate Program, University of California San Diego, 510-449-8870, joshchiou@ucsd.edu.

AUTHOR CONTRIBUTIONS

K.J.G and J.C. designed the study and wrote the manuscript. J.C. performed genetic association and single cell genomics analyses. R.G. performed molecular experiments of enhancer function. M.O. and S.Huang performed molecular experiments of variant function. R.M. and E.B. contributed to analyses of single cell gene expression. J.Y.H and M.M. generated single cell accessible chromatin data. P.B. and K.K. contributed to single cell motif enrichment analysis. D.U.G and S.P. supervised the generation of single cell accessible chromatin and contributed to data interpretation and analyses. M.S. supervised experiments related to enhancer function and contributed to data interpretation. S.Heller and A.K. contributed to design and interpretation of enhancer experiments.

CODE AVAILABILITY

Code used for processing snATAC-seq datasets and clustering cells is available at https://github.com/kjgaulton/pipelines/tree/master/T1D_snATAC_pipeline.

COMPETING INTERESTS

K.J.G is a consultant for Genentech and holds stock in Vertex Pharmaceuticals; neither is related to the work in this study. The other authors declare no competing interests.

ADDITIONAL INFORMATION

Supplementary Information is available for this paper.

and peripheral blood mononuclear cell types defined using single nucleus ATAC-seq (snATAC-seq) of 131,554 nuclei. T1D risk variants were enriched in cCREs active in T cells and additional cell types, including acinar and ductal cells of the exocrine pancreas. Risk variants at multiple T1D signals overlapped exocrine-specific cCREs linked to genes with exocrine-specific expression. At the *CFTR* locus, T1D risk variant rs7795896 mapped in a ductal-specific cCRE which regulated *CFTR*, and the risk allele reduced transcription factor binding, enhancer activity and *CFTR* expression in ductal cells. These findings support a role for the exocrine pancreas in T1D pathogenesis and highlight the power of large-scale GWAS and single cell epigenomics for understanding the cellular origins of complex disease.

Type 1 diabetes (T1D) is a complex autoimmune disease characterized by the loss of insulin-producing pancreatic beta cells³, where the triggers of autoimmunity and disease onset remain poorly understood. T1D has a strong genetic component, most prominently at the major histocompatibility complex (MHC) locus, but including 59 additional risk loci^{4–6}. T1D risk variants are largely non-coding, and intersection of risk variants with epigenomic data has identified enrichment within lymphoid enhancers⁴. However, due to limited sample sizes, incomplete variant coverage, and limited cell type resolution of existing epigenomic maps, the causal variants and cellular mechanisms of action of T1D risk loci are largely unresolved.

Discovery and fine-mapping of T1D loci

We performed a GWAS of 18,942 T1D cases and 501,638 controls of European ancestry from 9 cohorts (Supplementary Table 1). After applying uniform quality-control (Supplementary Figure 1), we imputed genotypes into the TOPMed reference panel and tested for T1D association⁷. Through meta-analysis, we combined association results for 61,947,369 variants and observed 81 loci reaching genome-wide significance ($P < 5 \times 10^{-8}$), including 48 of 59 known loci and 33 previously unreported loci (Figure 1a, Supplementary Figure 2, Supplementary Table 2). At 92 total loci (59 known and 33 novel), we discovered 44 independent signals, of which 36 were previously unreported (Figure 1b, Supplementary Figure 3). Nearly a third (32%; 29/92) of loci contained more than one signal; for example, the *PTPN2* and *BCL11A* loci each had three signals (Extended Data Figure 1).

We fine-mapped causal variants for 136 T1D signals including 92 main and 44 independent signals (Figure 1b). We obtained the posterior probability of association (PPA) for tested variants and defined 99% credible sets for each signal (Supplementary Table 3, Supplementary Data 1). Compared to a previous study⁸, fine-mapping resolution was improved based on credible set size and maximum posterior probability (Supplementary Figure 4). The median credible set size was 31 variants, where nearly a quarter (24%; 32/136) contained 5 or fewer variants, and 28% (38/136) contained a single variant with >0.50 PPA (Figure 1c). Credible sets at 15% (21/136) of signals contained a nonsynonymous variant with $PPA > 0.01$, including novel loci *AIRE* p.Arg471Cys ($PPA = 0.99$), *BATF3* p.Val11Ile ($PPA = 0.078$), *PRF1* p.Ala91Val ($PPA = 0.28$), and *INPP5B* p.Gly250Cys ($PPA = 0.055$) (Supplementary Table 4).

The TOPMed reference panel enables more accurate imputation of rare variants. We identified four novel variants with minor allele frequency (MAF) <0.005 and large effects on T1D (Extended Data Figure 2a). Among these, rs541856133 (MAF=0.0015, OR=3.01, 95% CI=2.33–3.89) mapped directly upstream of *CEL*, a gene implicated in maturity-onset diabetes of the young (MODY8)⁹. We also identified a novel protein-coding protective variant at *IFIH1* (p.Asn160Asp, rs75671397, MAF=0.002, OR=0.35, 95% CI=0.22–0.55) independent of known signals in this gene. Two additional non-coding risk variants mapped to *SH2B3* (rs570074821, MAF=0.0019, OR=1.89, 95% CI=1.37–2.61) and *CAMK4* (rs72663304, MAF=0.0013, OR=2.54, 95% CI=1.72–3.76) (Extended Data Figure 2b).

We characterized genetic correlations between T1D and other complex traits and diseases. Consistent with previous reports^{4,10}, T1D had significant (FDR <0.10) positive correlations with autoimmune diseases such as rheumatoid arthritis ($r_g=0.44$, FDR= 7.52×10^{-5}) and systemic lupus erythematosus ($r_g=0.35$, FDR= 5.05×10^{-7}), and negative correlation with ulcerative colitis ($r_g=-0.18$, FDR= 1.95×10^{-3}) (Extended Data Figure 3). We also observed positive correlations with metabolic traits such as fasting insulin level ($r_g=0.18$, FDR= 4.04×10^{-3}), coronary artery disease ($r_g=0.12$, FDR= 1.23×10^{-2}), and type 2 diabetes ($r_g=0.10$, FDR= 1.95×10^{-3}), and with pancreatic diseases such as pancreatic cancer ($r_g=0.25$, FDR= 1.11×10^{-1}) although this was just above significance. These results demonstrate relationships between genetic effects on T1D and autoimmune, metabolic and pancreatic disease.

Pancreas and immune cell gene regulation

The majority of T1D risk likely affects gene regulation⁴. To annotate T1D risk variants, we generated an accessible chromatin reference map using snATAC-seq of peripheral blood and pancreas from non-diabetic donors (Supplementary Table 5). We grouped chromatin accessibility profiles from 131,554 cells into 28 clusters (Figure 2a, Supplementary Figure 5a–c) and assigned cell type identities using chromatin accessibility at marker genes (Supplementary Table 6). For example, chromatin accessibility at *CIQB* marked pancreas tissue-resident macrophages, *REG1A* marked acinar cells, and *CFTR* marked ductal cells (Extended Data Figure 4a). We also observed patterns of chromatin accessibility at marker genes for cell sub-types, such as *FOXP3* for regulatory T cells (Extended Data Figure 4a). To relate cell type-resolved accessible chromatin to gene expression, we created a single cell RNA-seq (scRNA-seq) reference map of peripheral blood and pancreas. We assigned cell type identities for 90,495 cells to 29 clusters, which identified similar cell types and proportions as snATAC-seq (Extended Data Figure 5a–c).

To characterize *cis*-regulatory programs, we aggregated reads from cells within each snATAC-seq cluster and identified accessible chromatin peaks representing cCREs. There were 448,142 cCREs across all 28 clusters and an average of 77,812 cCREs per cluster (Supplementary Data 2). We also aggregated reads from cells within each scRNA-seq cluster to derive normalized expression (Supplementary Data 3). To delineate regulatory programs specifying each cell type, we identified 25,436 cCREs with accessibility patterns most specific to each cluster (Figure 2b, Supplementary Data 4). Genes within 100 kb of cell type-specific cCREs had more specific expression relative to other cCREs (Supplementary

Figure 6). Cell type-specific cCREs were also enriched for GO terms representing highly specialized cellular processes (Figure 2b, Supplementary Table 7).

We defined transcriptional regulators of cCRE activity by assessing transcription factor (TF) motif enrichment (Supplementary Data 5). Enriched TF motifs included those with lineage, cell type, and cell state specificity (Extended Data Figure 4b). As TFs within subfamilies often have similar motifs, we grouped TFs into subfamilies to identify TFs with matching expression and motif enrichment patterns (Supplementary Table 8). For example, FOXA subfamily TFs *FOXA2* and *FOXA3* were specifically expressed in pancreatic endocrine and exocrine cells, HNF1 subfamily TF *HNF1B* was specifically expressed in ductal cells, and ROR subfamily TF *RORC* was specifically expressed in memory CD8+ T cells (Extended Data Figure 4b, Supplementary Table 8).

As the target genes of cCRE activity are largely unknown, we identified cell type-resolved co-accessibility links between distal (non-promoter) cCREs and putative target gene promoters. Across all cell types, we observed 1,028,428 links (co-accessibility > 0.05) between distal cCREs and gene promoters (Supplementary Data 6). Co-accessible links were often cell type-specific; for example, distal cCREs were co-accessible with the *AQP1* promoter in ductal cells and the *CEL* promoter in acinar cells (Extended Data Figure 4c). In nearly every cell type, target genes co-accessible with distal cCREs were more likely to be expressed in the cell type compared to matched genes (Supplementary Figure 7).

Cell type annotation of T1D risk variants

We determined enrichment of variants associated with T1D and other complex traits and diseases for cell type cCREs. For T1D, the most significant enrichment was in T cell cCREs (naïve T $Z=5.57$, $FDR=2.26 \times 10^{-5}$; memory CD8+ T $Z=4.80$, $FDR=4.67 \times 10^{-4}$; activated CD4+ T $Z=4.62$, $FDR=6.74 \times 10^{-4}$; cytotoxic CD8+ T $Z=4.49$, $FDR=1.09 \times 10^{-3}$; regulatory T $Z=3.26$, $FDR=7.23 \times 10^{-3}$) and adaptive NK cells ($Z=3.50$, $FDR=9.93 \times 10^{-3}$) (Extended Data Figure 6). Notably, we did not observe enrichment in pancreatic resident immune cells (CD8+ T $Z=0.65$, $FDR=1.0$; macrophage $Z=-0.56$, $FDR=1.0$). Other immune-related diseases were primarily enriched within lymphocyte cCREs, while type 2 diabetes and glycemic traits were enriched in pancreatic endocrine, acinar, and ductal cCREs (Extended Data Figure 6). These results demonstrate that T1D variants are broadly enriched for T cell cCREs and highlight other traits enriched for pancreatic and immune cell cCREs.

Despite the strong enrichment of T1D-associated variants in T cells, many T1D signals did not overlap a T cell cCRE suggesting that additional cell types contribute to T1D risk. To identify additional disease-relevant cell types, we used an orthogonal approach to test for enrichment of T1D variants within the subset of cell type-specific cCREs. As expected, T1D-associated variants were enriched in cCREs specific to T cells and beta cells (activated CD4+ T $\ln(\text{enrich})=4.25$, 95% CI=1.11–5.43; cytotoxic CD8+ T $\ln(\text{enrich})=4.04$, 95% CI=0.20–5.20); INS^{high} beta cells ($\ln(\text{enrich})=3.58$, 95% CI=0.95–4.84) (Figure 3a). Interestingly, T1D variants were also enriched in cCREs specific to plasmacytoid dendritic (pDC) ($\ln(\text{enrich})=4.00$, 95% CI=1.96–5.10), classical monocytes

($\ln(\text{enrich})=3.78$, 95% CI=2.23–4.74), acinar ($\ln(\text{enrich})=3.35$, 95% CI=1.59–4.46) and ductal cells ($\ln(\text{enrich})=3.28$, 95% CI=0.18–4.69) (Figure 3a).

Given insight into key T1D-relevant cell types, we next annotated T1D signals in cCREs for these cell types. Over 75% (103/136) of T1D signals contained at least one variant ($\text{PPA}>0.01$) overlapping a cCRE, and at 65% (67/103) of these signals the cCRE was co-accessible with a gene promoter (Supplementary Table 9). Variants with high probabilities ($\text{PPA}>0.50$) were significantly more likely to map in a cCRE compared to other credible set variants ($\text{OR}=3.9$, 95% CI 1.9–7.8, $P=1.9\times 10^{-4}$), and these cCREs were more likely to be co-accessible with a promoter ($\text{OR}=6.1$, 95% CI 1.3–55.9, $P=7.1\times 10^{-3}$). For each signal, we calculated the cumulative posterior probability (cPPA) of credible set variants overlapping distal cCREs in each disease-enriched cell type. Numerous T1D signals had high cPPA in T cell cCREs and not in other disease-relevant cell types (Figure 3b). We also observed T1D signals with high cPPA in acinar and ductal (exocrine), beta cell, monocyte and pDC cCREs, several of which were highly cell type-specific (Figure 3b). For each signal, we further annotated genes within 1 Mb expressed in the same cell type and co-accessible with cCREs (Figure 3b, Supplementary Table 9).

Multiple T1D signals had high cPPA specifically in pancreatic exocrine cells and were linked to genes with exocrine-specific expression. At the *GP2* locus, three variants accounted for 0.951 PPA and mapped in an acinar-specific cCRE co-accessible with the promoter of *GP2*, which had acinar-specific expression (Figure 3b, Extended Data Figure 7a). Similarly, rs72802342 at the *BCAR1* locus ($\text{PPA}=0.30$) mapped in an acinar-specific cCRE co-accessible with the promoters of *CTRB1* and *CTRB2*, both of which had acinar-specific expression (Figure 3b, Extended Data Figure 7b). Other signals such as *CEL* had similar exocrine-specific profiles (Supplementary Figure 8a–c). Exocrine cCREs at T1D loci were also largely specific relative to stimulated immune cell and islet accessible chromatin (Supplementary Table 10).

T1D variant affects *CFTR* in ductal cells

The *CFTR* locus contained a fine-mapped variant rs7795896 ($\text{PPA}=0.63$) in a distal cCRE specific to ductal cells and co-accessible with the *CFTR* promoter in addition to other genes (Figure 4a). Recessive mutations in *CFTR* cause cystic fibrosis (CF), which is often comorbid with exocrine pancreas insufficiency and CF-related diabetes (CFRD)¹¹. Furthermore, carriers of *CFTR* mutations often develop chronic pancreatitis¹². As *CFTR* has not been implicated in T1D, we sought to validate the mechanism of this locus. The T1D risk allele of rs7795896 significantly reduced enhancer activity (594bp sequence two-sided ANOVA $P=1.15\times 10^{-2}$, Extended Data Figure 8a; 180bp sequence two-sided t-test $P=3.35\times 10^{-2}$, Extended Data Figure 8b) and reduced protein binding (bound fraction rs7795896-C=0.007, rs7795896-T=0.081; Extended Data Figure 8c, Supplementary Figure 9) in Capan-1 cells. The variant mapped in a sequence motif for HNF1B, albeit in a position predicted to minimally impact binding, and overlapped a HNF1B ChIP-seq site previously identified in ductal cells¹³ (Extended Data Figure 8d).

To determine whether the enhancer harboring rs7795896 regulated *CFTR* in ductal cells, we used CRISPR interference (CRISPRi) to inactivate enhancer activity (*CFTR*^{Enh}) in Capan-1 cells (Supplementary Table 11). As positive and negative controls, we inactivated the *CFTR* promoter (*CFTR*^{Prom}) and used a non-targeting guide RNA, respectively. Quantitative PCR revealed a significant reduction in *CFTR* expression after enhancer inactivation (two-sided ANOVA $P=1.77\times 10^{-4}$), whereas expression of other genes at the locus was unchanged (Figure 4b, Extended Data Figure 8e). We determined whether risk variants affected *CFTR* expression using pancreas eQTL data from GTEx¹⁴. Out of 13 tested genes, only *CFTR* had evidence for an eQTL ($P=4.31\times 10^{-4}$), which was colocalized with the T1D signal ($PP_{\text{shared}}=91.8\%$) (Extended Data Figure 9a). Among candidate variants with evidence for driving the shared signal using eCAVIAR ($CLPP>0.01$), only rs7795896 mapped in a cCRE. The T1D risk allele of rs7795896 was associated with decreased *CFTR* expression, consistent with effects on enhancer activity and TF binding. We re-calculated the eQTL association including estimated pancreas cell type proportion as an interaction term, and only ductal cells had significant association ($P=2.37\times 10^{-4}$) (Extended Data Figure 9b–d).

As *CFTR* has been implicated in pancreatic cancer¹⁵ and pancreatitis¹⁶, we asked whether rs7795896 was associated with these phenotypes in UK biobank and FinnGen. The T1D risk allele was associated with increased risk of pancreatitis (chronic pancreatitis $OR=1.15$, $P=3.18\times 10^{-3}$; acute pancreatitis $OR=1.07$, $P=1.15\times 10^{-2}$) and other pancreatic diseases ($OR=1.13$, $P=4.72\times 10^{-5}$) (Extended Data Figure 10a). In contrast, rs7795896 was not associated with other autoimmune diseases (all $P>0.05$). T1D signals associated with increased risk of pancreatic disease had significantly higher cPPA in exocrine cCREs compared to other signals (two-sided Student's t-test $P=0.027$) and no difference for T cell cCREs ($P=0.36$). Together, our findings support a model in which variants regulating *CFTR* and other genes in the exocrine pancreas increase risk of T1D and pancreatic diseases (Extended Data Figure 10b).

High-resolution mapping of both genetic variants influencing T1D risk and cell type-specific *cis*-regulatory programs in T1D-relevant tissues enabled new insight into disease mechanisms. Risk variants at multiple loci mapped to genes with specialized function in exocrine cells. While our results support variants in exocrine cCREs mediating T1D risk, fine-mapping has not resolved a single variant at most loci. Risk variants in exocrine-specific cCREs may also function in other cell types in the context of development, environmental changes, or disease progression. Continued fine-mapping in trans-ethnic cohorts with systematic evaluation of variant function in relevant cell types will further clarify risk mechanisms. Furthermore, as co-accessible links represent correlations that require both sites to vary in their accessibility, future studies will benefit from linking changes in chromatin to gene expression directly through single cell multi-omics.

Observational studies have reported exocrine pancreas abnormalities at T1D onset¹⁷, but it was unknown whether this was causing disease¹⁸. Genomic studies have also identified changes in exocrine cells in T1D^{19,20}. Exocrine pancreas abnormalities in T1D have been considered secondary to other disease processes, such as beta cell loss causing reduced insulinotropic effects on exocrine cells or viral infection leading to exocrine inflammation. In contrast, our findings provide evidence that exocrine cells intrinsically contribute to

T1D. Reduced *CFTR* leads to CFRD via intra-islet inflammation and immune infiltration, and immune infiltration in the exocrine pancreas has been suggested to contribute to T1D^{21–23}. Other implicated genes encode proteins secreted from acinar cells linked to risk of pancreatic disease^{24–26}, and may contribute to an inflammatory state. We therefore hypothesize a causal role for pancreatic exocrine gene regulation in T1D, which may provide novel avenues for therapeutic discovery.

METHODS

Genotype quality control and imputation

We compiled individual-level genotype data and summary statistics of 18,942 T1D cases and 501,638 controls of European ancestry from public sources (Supplementary Table 1), where T1D case cohorts were matched to population control cohorts based on genotyping array (Affymetrix, Illumina Infinium, Illumina Omni, and Immunochip) and country of origin where possible (US, British, and Ireland). For the GENIE-UK cohort, because we were unable to find a matched country of origin control cohort, we used individuals of British ancestry (defined by individuals within 1.5 interquartile range of CEU/GBR subpopulations on the first 4 PCs from PCA with European 1000 Genomes Project samples) from the University of Michigan Health and Retirement study (HRS). For non-UK Biobank cohorts, we first applied individual and variant exclusion lists (where available) to remove low quality, duplicate, or non-European ancestry samples and failed genotype calls for each cohort. For control cohorts, we also used phenotype files (where available) to remove individuals with type 2 diabetes or autoimmune diseases.

We then applied the HRC imputation preparation program (version 4.2.9) and used PLINK²⁷ (version 1.90b6.7) to remove variants based on (i) low frequency (MAF<1%), (ii) missing genotypes (missing>5%), (iii) violation of Hardy-Weinberg equilibrium (HWE $P < 1 \times 10^{-5}$ in control cohorts and HWE $P < 1 \times 10^{-10}$ in case cohorts), (iv) difference in allele frequency >0.2 compared to the Haplotype Reference Consortium r1.1 reference panel²⁸, and (v) allele ambiguity defined as AT/GC variants with MAF>40%³⁵. We further removed individuals based on (i) missing genotypes (missing>5%), (ii) sex mismatch with phenotype records ($\text{hom}_{\text{chrX}} > 0.2$ for females and $\text{hom}_{\text{chrX}} < 0.8$ for males), (iii) cryptic relatedness through identity-by-descent (IBD>0.2), and (iv) non-European ancestry through PCA with 1000 Genomes Project²⁹ (>3 interquartile range from 25th and 75th percentiles of European 1KGP samples on the first 4 PCs) (Supplementary Figure 1). Lists of independent variants for IBD and PCA calculations were generated using PLINK ('--indep 50 5 2'). For the affected sib-pair (ASP) cohort genotyped on the Immunochip, we retained only one T1D sample from each family selected at random. For the GRID case and 1958 Birth control cohorts genotyped on the Immunochip, a portion of the cases overlapped the T1DGC or 1958 Birth cohorts genotyped on a genome-wide array. We thus used sample IDs from the phenotype files to remove these samples from the GRID and 1958 Birth cohorts and verified that no samples were duplicated between the Immunochip and genome-wide array datasets by checking IBD. We combined data for matched case and control cohorts based on genotyping array and country of origin for imputation. We used the TOPMed Imputation Server³⁰ to impute genotypes into the TOPMed r2 panel⁷ and removed variants based on

low imputation quality ($R^2 < 0.3$). Following imputation, we implemented post-imputation filters to remove variants based on potential genotyping or imputation artifacts based on empirical R^2 (genotyped variants with empirical $R^2 < 0.5$ and all imputed variants in at least low linkage disequilibrium; LD, $r^2 > 0.3$).

For the UK Biobank cohort, we downloaded imputed genotype data from the UK Biobank v3 release which were imputed using a combination of the HRC and UK10K + 1000 Genomes reference panels. We removed individuals who had withdrawn participation from the UK biobank. We used phenotype data to remove individuals of non-European descent. To resolve duplicate samples represented in both the UK biobank and other cohorts on different genotyping arrays, we calculated IBD between samples in the UK biobank and cohorts of UK origin, removing duplicated samples from the UK biobank ($IBD > 0.9$). Following these filters, we then used a combination of ICD10 codes to define 1,445 T1D cases (T1D diagnosis, insulin treatment within a year of diagnosis, no T2D diagnosis). We defined controls as 362,050 individuals without diabetes (no T1D, T2D, or gestational diabetes diagnosis) or other autoimmune diseases (systemic lupus erythematosus, rheumatoid arthritis, juvenile arthritis, Sjögren syndrome, alopecia areata, multiple sclerosis, autoimmune thyroiditis, vitiligo, celiac disease, primary biliary cirrhosis, psoriasis, or ulcerative colitis). We removed variants with low imputation quality ($R^2 < 0.3$).

For the FinnGen cohort, we downloaded GWAS summary statistics for type 1 diabetes (T1D_STRICT) from FinnGen freeze 3 (<http://r3.finnngen.fi/>). This phenotype definition excluded individuals with type 2 diabetes from both cases and controls.

Association testing and meta-analysis

We tested variants with $MAF > 1 \times 10^{-5}$ for association to T1D with firth bias reduced logistic regression using EPACTS (<https://genome.sph.umich.edu/wiki/EPACTS>) for non-UK Biobank cohorts or SAIGE³¹ (version 0.38) for the UK Biobank, using genotype dosages adjusted for sex and the first four ancestry PCs. For the UK Biobank we used SAIGE as it is designed to run on biobank-scale cohorts and with highly imbalanced ratios of cases vs controls. For FinnGen, we used association results from the freeze 3 release that were generated using SAIGE. Prior to meta-analysis, we used liftOver to convert GRCh37/hg19 into GRCh38/hg38 coordinates for the UK biobank. We then combined association results across matched cohorts through inverse-variance weighted meta-analysis. We used liftOver to convert GRCh38/hg38 back into GRCh37/hg19 coordinates for the meta-analysis. We removed variants that were unable to be converted, were duplicated after coordinate conversion, or were located on different chromosomes after conversion. In total, our association data contained summary statistics for 61,947,369 variants. To evaluate the extent to which genomic inflation was driven by the polygenic nature of T1D or population stratification, we used LD score regression³² to compare the LDSC intercept to lambda genomic control (GC). We observed an intercept of 1.07 (SE=0.03) compared to a lambda GC of 1.20, suggesting that the majority of the observed inflation was driven by polygenicity rather than population stratification.

Stochastic search and fine-mapping of independent signals

We identified 59 loci (excluding the MHC locus) with T1D risk variants reported in previous genetic studies of T1D^{4–6,33}, and considered a locus in our study known if the most associated variant mapped within 500 kb of a previously reported T1D variant. We defined 33 novel loci where a variant reached genome-wide significance ($P < 5 \times 10^{-8}$), and both mapped at least 500 kb away and was not in LD ($r^2 < 0.01$) with a previously reported T1D variant. At 92 (59 known and 33 novel) loci, we defined the ‘index’ variant as the variant with strongest T1D association at the locus.

For all 92 loci, we used a 1 Mb window around the index variant as the region for fine-mapping using FINEMAP³⁴ (version 1.4). For each region, we first filtered for variants with $MAF > 0.0005$ and constructed pairwise LD matrices with PLINK²⁷ (‘--r --square --keep-allele-order’) using the TOPMed2-imputed cohorts with genome-wide coverage (DCCT-EDIC, GENIE-ROI, GENIE-UK, GoKinD, T1DGC, WTCCC1-T1D and their respective control cohorts). We then applied FINEMAP using these matrices to conduct shotgun stochastic search and Bayesian fine-mapping using the default prior (‘--sss --n-causal-snps 10 --prob-cred-set 0.99 --prior-std 0.05’). We selected the number of independent signals (causal variants) for each region based on the configuration with the highest FINEMAP posterior probability and used 99% credible sets from the FINEMAP output for the resulting signals. We calculated the effective sample size for all credible set variants, and no credible set variant with $PPA > 0.01$ had $< 50\%$ of the maximum effective sample size. We compared fine-mapping results to a previous fine-mapping dataset⁸. At 56 signals in common to both studies, we calculated the number of variants in the 99% credible set and the probability of the most likely causal variant.

GWAS correlation analyses

We used LD score regression^{32,35} (version 1.0.1) to estimate genome-wide genetic correlations between T1D and immune diseases^{36–44}, other diseases^{45–55}, and non-disease traits^{56–74}, using European subsets of GWAS where applicable. For acute pancreatitis, chronic pancreatitis, and pancreatic cancer, we used inverse variance weighted meta-analysis to combine SAIGE analysis results from the UK biobank³¹ (PheCodes 577.1, 577.2, and 157) and FinnGen r3 (K11_ACUTPANC, K11_CHRONPANC, C3_PANCREAS_EXALLC). We used pre-computed European 1000 Genomes LD scores to calculate correlation estimates (r_g) and standard errors. We then corrected p-values for multiple tests using FDR correction and considered $FDR < 0.1$ as significant. We also performed genetic correlation analyses using a version of the T1D meta-analysis excluding the ImmunoChip cohorts and observed highly similar results.

Generation of snATAC-seq libraries

Combinatorial indexing single cell ATAC-seq (snATAC-seq/sci-ATAC-seq).—snATAC-seq was performed as described previously^{75–77} with several modifications as described below. For the islet samples, approximately 3,000 islet equivalents (IEQ, roughly 1,000 cells each) were resuspended in 1 mL nuclei permeabilization buffer (10mM Tris-HCL (pH 7.5), 10mM NaCl, 3mM MgCl₂, 0.1% Tween-20 (Sigma), 0.1% IGEPAL-CA630 (Sigma) and 0.01% Digitonin (Promega) in water) and homogenized using 1mL glass

dounce homogenizer with a tight-fitting pestle for 15 strokes. Homogenized islets were incubated for 10 min at 4°C and filtered with 30 µm filter (CellTrics). For the pancreas samples, frozen tissue was pulverized with a mortar and pestle while frozen and immersed in liquid nitrogen. Approximately 22 mg of pulverized tissue was then transferred to an Eppendorf tube and resuspended in 1 mL of cold permeabilization buffer for 10 minutes on a rotator at 4°C. Permeabilized sample was filtered with a 30µm filter (CellTrics), and the filter was washed with 300 µL of permeabilization buffer to increase nuclei recovery.

Once permeabilized and filtered, nuclei were pelleted with a swinging bucket centrifuge (500×g, 5 min, 4°C; 5920R, Eppendorf) and resuspended in 500 µL high salt tagmentation buffer (36.3 mM Tris-acetate (pH = 7.8), 72.6 mM potassium-acetate, 11 mM Mg-acetate, 17.6% DMF) and counted using a hemocytometer. Concentration was adjusted to 4500 nuclei/9 µL, and 4,500 nuclei were dispensed into each well of a 96-well plate. Glycerol was added to the leftover nuclei suspension for a final concentration of 25 % and nuclei were stored at -80°C. For tagmentation, 1 µL barcoded Tn5 transposomes were added using a BenchSmart™ 96 (Mettler Toledo), mixed five times and incubated for 60 min at 37°C with shaking (500 rpm). To inhibit the Tn5 reaction, 10 µL of 40 mM EDTA were added to each well with a BenchSmart™ 96 (Mettler Toledo) and the plate was incubated at 37°C for 15 min with shaking (500 rpm). Next, 20 µL 2 x sort buffer (2 % BSA, 2 mM EDTA in PBS) were added using a BenchSmart™ 96 (Mettler Toledo). All wells were combined into a FACS tube and stained with 3 µM Draq7 (Cell Signaling). Using a SH800 (Sony), 20 nuclei were sorted per well into eight 96-well plates (total of 768 wells) containing 10.5 µL EB (25 pmol primer i7, 25 pmol primer i5, 200 ng BSA (Sigma)). Preparation of sort plates and all downstream pipetting steps were performed on a Biomek i7 Automated Workstation (Beckman Coulter). After addition of 1 µL 0.2% SDS, samples were incubated at 55°C for 7 min with shaking (500 rpm). We added 1 µL 12.5% Triton-X to each well to quench the SDS and 12.5 µL NEBNext High-Fidelity 2× PCR Master Mix (NEB). Samples were PCR-amplified (72°C 5 min, 98°C 30 s, (98°C 10 s, 63°C 30 s, 72°C 60 s) × 12 cycles, held at 12°C). After PCR, all wells were combined. Libraries were purified according to the MinElute PCR Purification Kit manual (Qiagen) using a vacuum manifold (QIAvac 24 plus, Qiagen) and size selection was performed with SPRI Beads (Beckmann Coulter, 0.55x and 1.5x). Libraries were purified one more time with SPRI Beads (Beckmann Coulter, 1.5x). Libraries were quantified using a Qubit fluorimeter (Life technologies) and the nucleosomal pattern was verified using a TapeStation (High Sensitivity D1000, Agilent). The library was sequenced on a HiSeq2500 sequencer (Illumina) using custom sequencing primers, 25% spike-in library and following read lengths: 50+43+40+50 (Read1+Index1+Index2+Read2).

Droplet-based 10x single cell ATAC-seq (scATAC-seq).—10x scATAC-seq protocol from 10x Genomics was followed: Chromium SingleCell ATAC ReagentKits UserGuide (CG000209, Rev A). Cryopreserved PBMC samples were thawed in 37°C water bath for 2 min and followed ‘PBMC thawing protocol’ in the UserGuide. After thawing cells, the pellets were resuspended again in 1 mL chilled PBS (with 0.04% PBS) and filtered with 50 µm CellTrics (04-0042-2317, Sysmex). The cells were centrifuged (300×g, 5 min, 4°C) and permeabilized with 100 µl of chilled lysis buffer (10 mM Tris-HCl pH 7.4, 10 mM NaCl, 3 mM MgCl₂, 0.1% Tween-20, 0.1% IGEPAL-CA630, 0.01% digitonin and 1%

BSA). The samples were incubated on ice for 3 min and resuspended with 1mL chilled wash buffer (10 mM Tris-HCl pH 7.4, 10 mM NaCl, 3 mM MgCl₂, 0.1% Tween-20 and 1% BSA). After centrifugation (500×g, 5 min, 4°C), the pellets were resuspended in 100 µL of chilled Nuclei buffer (2000153, 10x Genomics). The nuclei concentration was adjusted between 3,000 to 7,000 per µl and 15,300 nuclei which targets 10,000 nuclei was used for the experiment. For pancreas tissue (pulverized as described above), approximately 31.7 mg of pulverized tissue was transferred to a LoBind tube (Eppendorf) and resuspended in 1 mL of cold permeabilization buffer (10mM Tris-HCL (pH 7.5), 10mM NaCl, 3mM MgCl₂, 0.1% Tween-20 (Sigma), 0.1% IGEPAL-CA630 (Sigma), 0.01% Digitonin (Promega) and 1% BSA (Proliant 7500804) in water) for 10 min on a rotator at 4°C. Permeabilized nuclei were filtered with 30 µm filter (CellTrics). Filtered nuclei were pelleted with a swinging bucket centrifuge (500×g, 5 min, 4°C; 5920R, Eppendorf) and resuspended in 1 mL Wash buffer (10mM Tris-HCL (pH 7.5), 10mM NaCl, 3mM MgCl₂, 0.1% Tween-20, and 1% BSA (Proliant 7500804) in molecular biology-grade water). Nuclei wash was repeated once. Next, washed nuclei were resuspended in 30 µL of 1X Nuclei Buffer (10X Genomics). Nuclei were counted using a hemocytometer, and finally the nuclei concentration was adjusted to 3,000 nuclei/µL. 15,360 nuclei were used as input for tagmentation.

Nuclei were diluted to 5 µl with 1X Nuclei buffer (10x Genomics) and, mixed with ATAC buffer (10x Genomics) and ATAC enzyme (10x Genomics) for tagmentation (60 min, 37°C). Single cell ATAC-seq libraries were generated using the (Chromium Chip E Single Cell ATAC kit (10x Genomics, 1000086) and indexes (Chromium i7 Multiplex Kit N, Set A, 10x Genomics, 1000084) following manufacturer instructions. Final libraries were quantified using a Qubit fluorimeter (Life technologies) and the nucleosomal pattern was verified using a TapeStation (High Sensitivity D1000, Agilent). Libraries were sequenced on a NextSeq 500 and HiSeq 4000 sequencer (Illumina) with following read lengths: 50+8+16+50 (Read1+Index1+Index2+Read2).

Single cell chromatin accessibility data processing

Prior to read alignment, we used trim_galore (version 0.4.4) to remove adapter sequences from reads using default parameters. For combinatorial barcoding data, we aligned reads to the hg19 reference genome using bwa mem⁷⁸ (version 0.7.17-r1188; '-M -C') and removed low mapping quality (MAPQ<30), secondary, unmapped, and mitochondrial reads using samtools⁷⁹ (version 1.10). To remove duplicate sequences on a per-barcode level, we used the MarkDuplicates tool from picard ('BARCODE_TAG'). For droplet-based 10x data, we used Cell Ranger ATAC (version 1.1.0) to process, align, and remove duplicate reads. For each tissue and snATAC-seq technology, we used log-transformed read depth distributions from each experiment to determine a threshold separating real cell barcodes from background noise. We used >500 total reads for combinatorial barcoding snATAC-seq and >2,300–4,000 total reads, as well as >0.3 fraction of reads in peaks for 10x snATAC-seq experiments (Supplementary Figure 7a).

Single cell chromatin accessibility clustering

We identified snATAC-seq clusters using a previously described pipeline with a few modifications⁷⁵. For each experiment, we first constructed a counts matrix consisting of read

counts in 5 kb windows for each cell. Using scanpy⁸⁰ (version 1.4.4.post1), we normalized cells to a uniform read depth and log-transformed counts. We extracted highly variable (*h_v*) windows ('min_mean=0.01, min_disp=0.25') and regressed out the total log-transformed read depth within *h_v* windows (usable counts). We then merged datasets from the same tissue and performed PCA to extract the top 50 PCs. We used Harmony⁸¹ (version 1.0) to correct the PCs for batch effects across experiments, using categorical covariates including donor-of-origin, biological sex, and snATAC-seq assay technology. We used the corrected components to construct a 30 nearest neighbor graph using the cosine metric, which we used for UMAP dimensionality reduction ('min_dist=0.3') and clustering with the Leiden algorithm⁸² ('resolution=1.5').

Prior to combining cells across all tissues, we performed iterative clustering to identify and remove cells with low fraction of reads in peaks (using preliminary peaks called from data in bulk) or low usable counts (islets: 948, pancreas: 2,588, PBMCs: 5,268 cells removed in total). Next, after removing low-quality cells and repeating the previous clustering steps, we sub-clustered the resulting main clusters at high resolution ('resolution=3.0') to identify sub-clusters containing potential doublets (islets: 886, pancreas: 4,495, PBMCs: 5,844 cells removed in total). We noted that these sub-clusters tended to have higher average usable counts, promoter usage, and accessibility at more than one marker gene promoter. After removing 20,029 low-quality or potential doublet cells, we performed a final round of clustering using experiments from all tissues, including tissue-of-origin as another covariate. We further removed 672 cells mapping to improbable cluster assignments (islet or pancreatic cells in PBMC clusters or vice versa). After all filters, we ended up with 131,554 cells mapping to 28 distinct clusters with consistent representation across samples from the same tissue (Supplementary Figure 7b). We cataloged known marker genes for each cell type using a combination of literature search and PanglaoDB⁸³ (Supplementary Table 6) and assessed gene accessibility (sum of read counts across each gene body) to assign labels to each cluster.

Single cell gene expression clustering

We compiled publicly available scRNA-seq datasets of peripheral blood (10x Genomics; v1 Chemistry – 3k, 6k, and 33k; v2 Chemistry – 4k and 8k, v3 Chemistry – 5k and 10k, v3.1 Chemistry – 5k, 10k single indexed, and 10k dual indexed) and pancreatic islets⁸⁴. We re-processed each dataset using Cell Ranger RNA (version 4.0.0) with the GRCh37 reference genome and removed cells with <500 genes expressed (non-zero counts). We extracted *h_v* genes for PBMCs and pancreatic islets separately and merged both lists to obtain a single set of *h_v* genes. For each sample, we used count matrices as input for scanpy⁸⁰ (version 1.4.4.post1), normalized counts for each cell to uniform read depth, log-transformed the normalized counts, and regressed out the log total counts for *h_v* genes. We then merged all datasets and extracted the top 100 PCs using PCA. We used Harmony⁸¹ (version 1.0) to correct PCs for covariates including the experiment, donor, tissue, and biological sex. We constructed a 30 nearest neighbor graph using the cosine metric, performed UMAP dimensionality reduction ('min_dist=0.3'), and clustered with the Leiden algorithm⁸² ('resolution=1.25'). We performed iterative clustering to remove 10,014 low quality and 5,286 potential doublet cells, leaving 90,495 cells for the cell type-resolved

expression reference map. We used a combination of literature search and PanglaoDB⁸³ (Supplementary Table 6) to assign labels to each cluster. For each cell type, we normalized aggregated reads from individual cells to derive TPM for each gene.

Cataloging cell type-resolved cCREs

We identified chromatin accessibility peaks with MACS2⁸⁵ (version 2.1.2) by calling peaks on aggregated reads from each cluster. In brief, we extracted reads from all cells within a given cluster, shifted reads aligned to the positive strand by +4 bp and reads aligned to the negative strand by -5 bp, and centered the reads. We then used MACS2 to call peaks ('--nomodel --keep-dup-all') and removed peaks overlapping ENCODE blacklisted regions^{2,86}. We then merged peaks from all 28 clusters with bedtools⁸⁷ (version 2.26.0) to create a consistent set of 448,142 cCREs for subsequent analyses.

To compare accessible chromatin profiles from snATAC-seq to those from bulk ATAC-seq on FACS purified cell types, we reprocessed published ATAC-seq data from sorted pancreatic⁸⁸ and unstimulated immune cells⁸⁹. We created pseudobulk profiles from the snATAC-seq data for each donor and cluster, retaining those that contained information from >50 cells. We then extracted read counts in the 448,142 cCREs for all sorted and pseudobulk profiles. We used PCA to extract the top 20 principal components and used UMAP for dimensionality reduction and visualization ('min_dist=0.5, n_neighbors=80').

Defining cell type-specific cCREs

To identify cCREs with accessibility levels most specific to each cluster, we used logistic regression models for each cCRE treating each cell as an individual data point. We performed separate regressions for each cluster, with binary cluster assignment and the covariates donor-of-origin and the log usable count as predictors and binary accessibility of the peak as the outcome, to calculate chromatin accessibility (CA) t-statistics. For a given cluster, we defined cCREs with activity most specific to that cluster by taking the top 1000 cCREs with the highest CA t-statistics, after first filtering out cCREs which also had high CA t-statistics for other clusters (cCRE cell type CA t-statistics > 90th percentile in >2 other cell types). The cCREs were all significant after Bonferroni correction for the number of peaks ($P < 1.1 \times 10^{-7}$) except for pancreatic CD8+ T (n=428 after correction), regulatory T (n=347) and memory CD8+ T (n=175). We then used GREAT⁹⁰ (version 3) to annotate gene ontology terms enriched in each set of cell type-specific cCREs compared to a background of all cCREs.

To assess whether cell type-specific cCREs tended to be close in proximity to genes with cell type-specific expression, we defined 100 kb windows around the midpoint of each cell type-specific cCRE and annotated genes with overlapping TSS. For each cell type that had a corresponding cluster in scRNA-seq, we compared whether genes around cell type-specific cCREs for that cell type had higher gene expression specificity scores than the rest of the cell type-specific cCREs using two-sided Welch's t-tests. We collapsed cell type-specific cCREs for cell types with more than one state in snATAC-seq but only one state in scRNA-seq.

Comparing single cell chromatin accessibility and gene expression clusters

To compare cell types from snATAC-seq and scRNA-seq, we first derived gene expression t-statistics for each gene using linear regression models separately for each cluster of log-transformed read count as a function of binary cluster assignment, donor-of-origin, and log sequencing depth, treating cells as individual data points. For each gene, we also used chromatin accessibility t-statistics for promoter cCREs (see “Defining cell type-specific cCREs”). For each scRNA-seq cluster, we extracted the top 100 most specific genes based on the gene expression t-statistic. Using a merged list of the most specific genes across all clusters, we compared gene expression and promoter accessibility t-statistics using Pearson correlation.

Single cell motif enrichment

We estimated TF motif enrichment z-scores for each cell using chromVAR⁹¹ (version 1.5.0) by following the steps outlined in the user manual. First, we constructed a sparse binary matrix encoding read overlap with merged peaks for each cell. For each merged peak, we estimated the GC content bias to obtain a set of matched background peaks. To ensure a motif enrichment value for each cell, we did not apply any additional filters based on total reads or the fraction of reads in peaks. Next, using 580 TF motifs within the JASPAR 2018 CORE vertebrate (non-redundant) set⁹², we computed GC bias-corrected enrichment z-scores (chromVAR deviation scores) for each cell. For each cell type, we considered a TF motif enriched if the average z-score across cells was greater than 2. We used the TFClass database⁹³ (<http://tfclass.bioinf.med.uni-goettingen.de/>) to group enriched TF motifs into structural sub-families. We determined the expression of all TFs within the subfamily in each cell type identified in scRNA-seq and considered TFs expressed in a cell type with TPM>1.

Single cell co-accessibility

We used Cicero⁹⁴ (version 1.3.3) to calculate co-accessibility scores between pairs of peaks for each cluster. As in the single cell motif enrichment analysis, we started from a sparse binary matrix. For each cluster, we only retained merged peaks that overlapped peaks from the cluster. Within each cluster, we aggregated cells based on the 50 nearest neighbors and used cicero to calculate co-accessibility scores, using a 1 Mb window size and a distance constraint of 500 kb. We then defined promoters as ± 500 bp from the TSS of protein coding transcripts from GENCODE v19⁹⁵ to annotate co-accessibility links between gene promoters and distal cCREs (non-promoter cCREs).

To assess whether genes with co-accessible links between the promoter and distal cCREs (co-accessible genes; co-accessibility score>0.05) were expressed more often than non-co-accessible genes (co-accessibility score<0) within each cell type, we separated co-accessible links into bins based on the distance between the gene promoter and distal cCRE. Within each bin, we then compared the fraction of genes expressed in the cell type (TPM>1 from scRNA-seq) between co-accessible and non-co-accessible genes using 2-sided Fisher’s exact tests. We collapsed co-accessible links for cell types with more than one state in snATAC-seq but only one state in scRNA-seq (alpha, beta, and delta cells). No comparison was made for pancreatic CD8+ T cells, which did not have a corresponding cluster in scRNA-seq.

GWAS enrichment analyses

We used LD score regression^{32,96,97} (version 1.0.1) to calculate genome-wide enrichment z-scores for 32 diseases and traits including T1D. We obtained GWAS summary statistics for autoimmune and inflammatory diseases (immune-related)^{36–44}, other diseases^{45–53}, and quantitative endophenotypes^{56–65}, and where necessary, we filled in variant IDs and alleles. Using ‘munge_sumstats.py’, we converted summary statistics to the LD score regression standard format. For each cluster, we considered overlap with chromatin accessibility peaks as a binary annotation for variants. Then, we computed annotation-specific LD scores by following the instructions for creating partitioned LD scores. We estimated enrichment coefficient z-scores for each annotation relative to the background annotations in the baseline-LD model (version 2.2). Using the enrichment z-scores, we computed two-sided p-values to assess significance and corrected for multiple tests using the Benjamini-Hochberg procedure. We also calculated GWAS enrichment z-scores for T1D using a version of the meta-analysis excluding the ImmunoChip cohorts and observed highly similar enrichment results.

From the full GWAS summary statistics, we first extracted variants with MAF>0.05 and calculated approximate Bayes factors⁹⁸ for each variant, assuming prior variance in allelic effects = 0.04. We then used fgwas⁹⁹ (version 0.3.6) to estimate T1D enrichment for common variants (MAF>0.05) within cell type-specific cCREs using an average window size of 1 Mb also including annotations for coding exons, 3’/5’UTR regions and 1 kb upstream of the transcription start site (TSS) from GENCODE in each model. We considered cell type annotations enriched where $\ln(95\% \text{ CI lower bound}) > 0$ and depleted where $\ln(95\% \text{ CI upper bound}) < 0$.

Annotating cell type mechanisms of variants at fine mapped signals

We compared the proportion of credible set variants with PPA>0.50 overlapping a cCRE compared to other credible set variants using a two-sided Fisher’s exact test. Among credible set variants in cCREs, we further compared the proportion of credible set variants with PPA>0.50 in a cCRE co-accessible with a gene promoter compared to other credible set variants using a two-sided Fisher’s exact test.

For each T1D signal, we calculated the cumulative posterior probability of all credible set variants overlapping cCREs active in T cells, monocytes, plasmacytoid dendritic cells, beta cells, acinar cells and ductal cells. For each signal overlapping cCREs, we annotated genes within 1 Mb of the index variant that were (i) expressed in the same cell type(s) (TPM>1 from scRNA-seq) and (ii) co-accessible with a cCRE harboring a credible set variant with PPA>0.01.

Luciferase reporter assays

We tested for allelic differences in enhancer activity at rs7795896 using multiple constructs. First, we cloned a 180 bp sequence of human DNA (Coriell) containing the reference or alternate allele into the luciferase reporter vector pGL4.23 (Promega) in the forward direction using the restriction enzymes SacI and KpnI. Second, we cloned a larger 594 bp sequence of human DNA (Coriell) containing the rs7795896 reference allele corresponding

to the coordinates of the ductal-specific cCRE into pGL4.23 in the forward direction using the restriction enzymes SacI and KpnI. We introduced the alternate allele via SDM using the NEB Q5 Site Directed Mutagenesis kit (New England Biolabs) on 1 ng plasmid containing the reference allele and primers designed using the NEBaseChanger v.1.2.8 software. Sequence identity for all plasmids was confirmed with Sanger sequencing using the RV3 primer. Cloning primers were designed using Primer3 version 0.4.0. Primer sequences for cloning and SDM are listed in Supplementary Table 11.

We obtained Capan-1 cells from ATCC, and cells were authenticated by ATCC using karyotyping, morphology and PCR-based approaches. Cells tested negative for mycoplasma contamination. We grew Capan-1 cells, a model for ductal cells¹⁰⁰, to approximately 70% confluency according to ATCC culture recommendations in 6-well or 24-well plates and fed complete growth media the day before transfection. For the 180bp construct, 2500 ng experimental or empty (pGL4.23) vector was co-transfected with 50 ng pRL-SV40 per sample using Lipofectamine 3000 (Invitrogen) into Capan-1 cells grown in a 6-well plate. For the 594 bp construct, 500 ng experimental or empty vector was co-transfected with 10 ng pRL-TK per sample using Lipofectamine 3000 (Invitrogen) into Capan-1 cells grown in a 24-well plate. The experiment was also repeated using 50 ng pRL-TK per sample. For all experiments, 48 hours post-transfection samples were assayed using the Dual-Glo Luciferase Assay System (Promega). We normalized Firefly:Renilla ratios with respect to the empty vector and used either two-sided, two-way ANOVA or two-sided Student's T-test to compare luciferase activity between the two alleles.

Electrophoretic mobility shift assay

We ordered double-stranded 5' biotinylated and corresponding unlabeled (cold) oligonucleotides of 16 bp centered on rs7795896 with the reference and alternate alleles from Integrated DNA Technologies. Oligo sequences are listed in Supplementary Table 11. We performed EMSA using the LightShift Chemiluminescent EMSA kit (Thermo Fisher) according to manufacturer's instructions with the following adjustments: 100 fmol of biotinylated duplex probe per reaction, and 20 pmol of the same-allele non-biotinylated duplex "cold" probe in competition reactions (200× molar excess of the biotin probe). We used the NE-PER Nuclear Protein and Cytoplasmic Extraction Reagents (Thermo Fisher) kit to extract nuclear protein from Capan-1 cells and used 2uL of nuclear extract per binding reaction, corresponding to approximately 5–15ug of nuclear protein per reaction. We quantified bound and free probe (unbound) band intensity using ImageJ (v.1.53) and calculated the ratio of bound to unbound intensity. We then averaged bound ratios for replicates of each allele and compared ratios between alleles.

CRISPR inactivation of enhancer element

We obtained HEK293T cells from ATCC, and cells were authenticated by ATCC using karyotyping, morphology and PCR-based approaches. Cells tested negative for mycoplasma contamination. We maintained HEK293T cells in DMEM containing 100 units/mL penicillin and 100 mg/mL streptomycin sulfate supplemented with 10% fetal bovine serum. To generate CRISPRi lentiviral expression vectors, we designed guide RNA sequences to target the enhancer containing rs7795896 or the *CFTR* promoter. These guide RNAs,

as well as a non-targeting control guide RNA, were placed downstream of the human U6 promoter in the pLV hU6-sgRNA hUbc-dCas9-KRAB-T2a-Puro backbone (Addgene, plasmid #71236). Targeting guide RNAs were designed using Benchling and selected to maximize both on-target binding¹⁰¹ and guide specificity¹⁰². The non-targeting control guide RNA was selected from a previously validated genome-wide library¹⁰³. Guide RNA sequences and targeted regions are listed in Supplementary Table 11. Higher scores indicate greater on-target binding and specificity.

We generated high-titer lentiviral supernatants by co-transfection of the resulting plasmid and lentiviral packaging constructs into HEK293T cells. Specifically, we co-transfected CRISPRi vectors with the pCMV-R8.74 (Addgene, #22036) and pMD2.G (Addgene, #12259) expression plasmids into HEK293T cells using a 1mg/ml PEI solution (Polysciences). We collected lentiviral supernatants at 48 and 72 hours after transfection and concentrated lentiviruses by ultracentrifugation for 120 min at 19,500 rpm using a Beckman SW28 ultracentrifuge rotor at 4°C. Lentiviral titers were subsequently determined using a qPCR Lentivirus Titer Kit (Abm Bio), and aliquots were stored at -80°C.

We obtained Capan-1 pancreatic ductal adenocarcinoma cell lines from ATCC and cultured using Iscove's Modified Dulbecco's Media with 20% fetal bovine serum, 100 units/mL penicillin, and 100 mg/mL streptomycin sulfate. 24 hours prior to transduction, we passaged cells into a 12-well plate at a density of 100,000 cells per well. The following day, we added fresh medium containing 8µg/mL polybrene and concentrated CRISPRi lentivirus at an MOI of 40 to each well. For each condition (1 non-targeting guide RNA, 3 enhancer-targeting guide RNAs, and 1 promoter-targeting guide RNA) we transduced 3 wells for a total of 15 wells. We additionally included 3 wells of mock-transduced cells without lentivirus. We incubated the cells at 37°C for 30 minutes and then spun them in a centrifuge for 1 hour at 30°C at 950×g. 6 hours later, we replaced viral medium with fresh base culture medium for cell recovery. After 48 hours, we replaced medium daily with the addition of 1µg/mL puromycin for an additional 72 hours, at which point all mock-transduced cells were killed. We reduced the concentration of puromycin to 0.5 µg/mL and cultured cells with daily medium changes for an additional week before passaging each cell line into a 48-well plate at a density of approximately 100,000 cells per well. The following morning, we harvested cells from each condition and isolated RNA using the RNeasy[®] Micro Kit (Qiagen) according to the manufacturer's instructions.

For qRT-PCR, we performed cDNA synthesis using the iScript[™] cDNA Synthesis Kit (Bio-Rad) and 250 ng of isolated RNA per reaction. We performed qRT-PCR reactions in triplicate with 5 ng of template cDNA per reaction using a CFX96[™] Real-Time PCR Detection System and the iQ[™] SYBR[®] Green Supermix (Bio-Rad). We used PCR of the TATA binding protein (TBP) coding sequence as an internal control, quantified relative expression via double delta CT analysis, and compared relative expression using two-sided ANOVA (enhancer inactivation versus non-targeting control) or a two-sided Student's t-test (promoter inactivation versus non-targeting control). Genes with CT values greater than 34 were considered as not expressed. We also evaluated changes in expression of the puromycin resistance gene and the dCAS9 gene as additional controls. For eukaryotic genes, each

primer pair was designed to span an exon-exon junction. Primers used for qPCR are listed in Supplementary Table 11.

Colocalization and deconvolution of the pancreas *CFTR* eQTL

We obtained GTEx v7¹⁴ eQTL summary statistics for pancreas tissue from 220 samples and used effect size (beta) and standard error estimates from the regression model for *CFTR* expression to calculate approximate Bayes factors⁹⁸ for each variant, assuming prior variance in allelic effects = 0.04. We considered all variants in a 500 kb window around the T1D index variant at *CFTR* (rs7795896) tested in both the GWAS and eQTL datasets and used coloc¹⁰⁴ (version 4.0.4) to calculate the probability that the variants driving T1D and eQTL signals were shared, using prior probabilities $PP_{T1D}=1\times 10^{-4}$, $PP_{eQTL}=1\times 10^{-4}$, and $PP_{shared}=1\times 10^{-5}$. We considered the T1D and *CFTR* eQTL signals colocalized based on the probability that they were shared (PP_{shared}) >0.9. We applied eCAVIAR¹⁰⁵ (version 2.2) using variants in a 500 kb window tested for both T1D and eQTL association using LD calculated from EUR samples in 1000 Genomes²⁹ and considered variants with $CLPP>0.01$ to be candidate causal variants for a shared signal.

We used MuSiC¹⁰⁶ (version 0.1.1) to estimate the proportions of major pancreatic cell types (acinar, duct, stellate, alpha, beta, delta, gamma) in each GTEx v7 pancreas sample. As input, we used raw count matrices from scRNA-seq of pancreatic cell types with labels from the gene expression reference map and GTEx v7 pancreas samples. For each cell type, we used the proportion as an interaction term and constructed linear models of TMM-normalized *CFTR* expression as a function of the interaction between genotype dosage and cell type proportion, accounting for covariates used by GTEx including sex, sequencing platform, 3 genotype PCs, and 28 inferred PCs from the expression data. From the original 30 inferred PCs, we excluded inferred PCs 2 and 3 because they were highly correlated with acinar cell proportion (Spearman's $\rho>0.7$). No remaining PCs were highly correlated (Spearman's $\rho<0.3$) with the proportions of other cell types.

Phenotype associations at T1D signals

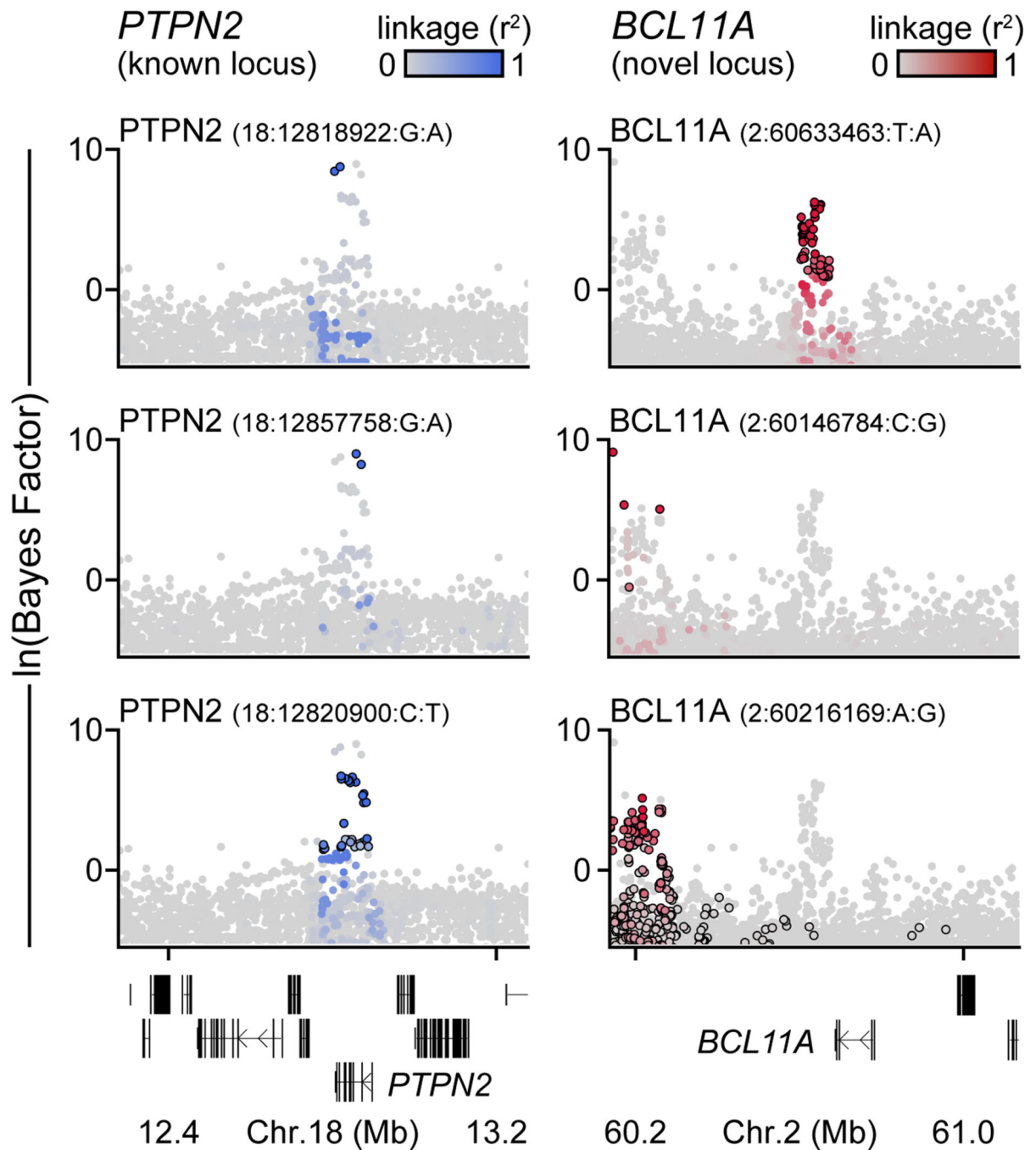
We tested association of the T1D index variant at *CFTR* (rs7795896) for pancreatic and autoimmune disease phenotypes. For acute pancreatitis, chronic pancreatitis, and pancreatic cancer, we used inverse variance weighted meta-analysis to combine SAIGE analysis results from the UK biobank³¹ (PheCodes 577.1, 577.2, and 157) and FinnGen (K11_ACUTPANC, K11_CHRONPANC, C3_PANCREAS_EXALLC). As mutations that cause cystic fibrosis (CF) map to this locus, which are risk factors for pancreatitis and pancreatic cancer, we determined the impact of the most common CF mutation F508del/rs199826652 on the association results for rs7795896. For T1D, we tested for association of rs7795896 conditional on F508del/rs199826652 in all cohorts except for FinnGen and observed no evidence for a difference in T1D association. For pancreatitis and pancreatic cancer, we identified F508del/rs199826652 carriers in UK Biobank and repeated the association analysis for these phenotypes in UK biobank data after removing these individuals and observed no evidence of a change in the effect of rs7795896.

We identified T1D signals where the risk allele had at least nominal association ($P < 0.05$) with increased risk of acute pancreatitis, chronic pancreatitis, or pancreatic cancer. We then tested whether these T1D signals had a difference in cPPA in exocrine cell cCREs or T cell cCREs compared to other T1D signals using a two-sided Student's T-test.

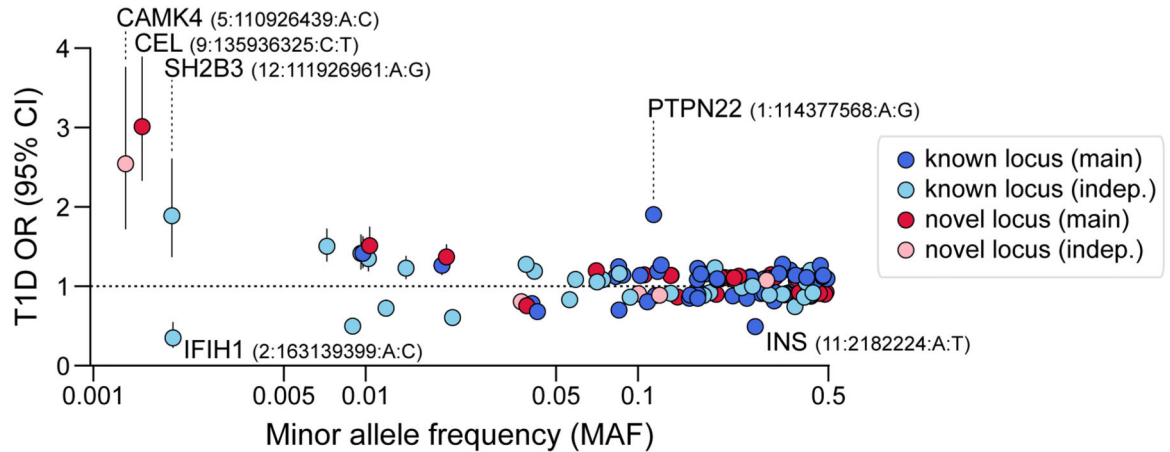
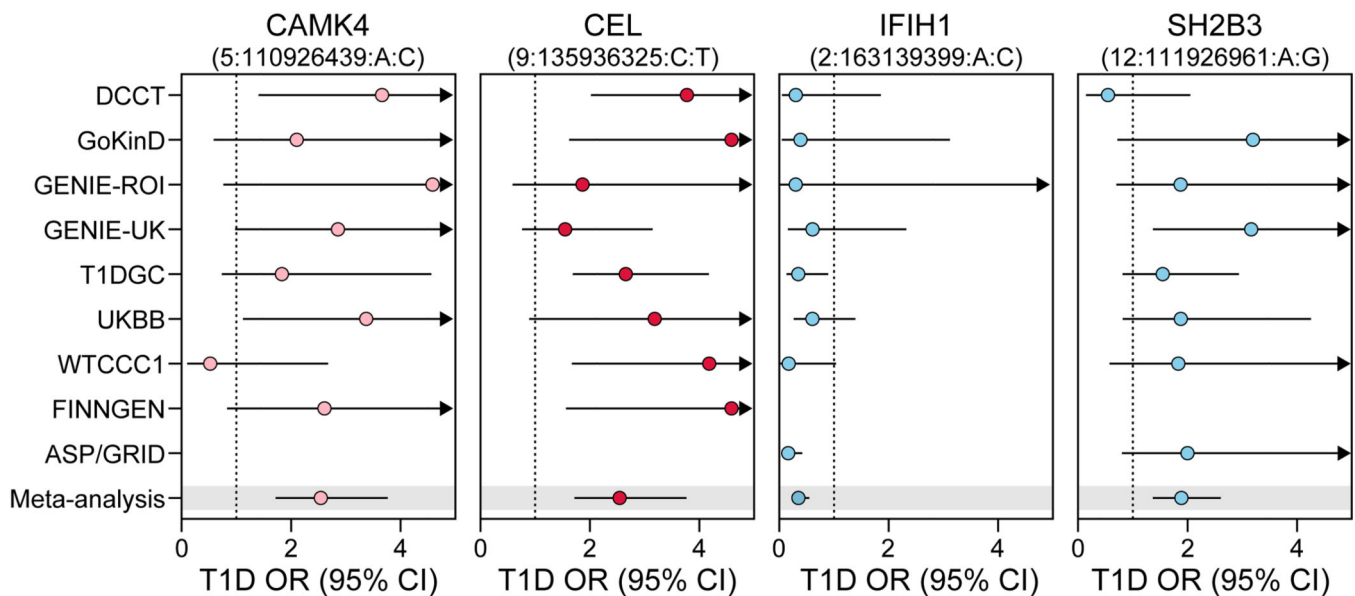
Human participant ethics

Genotype data obtained from dbGAP, WTCCC, and UK Biobank were used in accordance with approved research plans for these data as obtained from the respective data repositories. Tissue samples for pancreas and peripheral blood were obtained from external biorepositories nPOD and Hemacare, and all individuals gave consent for the use of tissue samples. All genotype data and tissue samples were de-identified prior to being obtained and all studies were approved by the Institutional Review Board of UCSD.

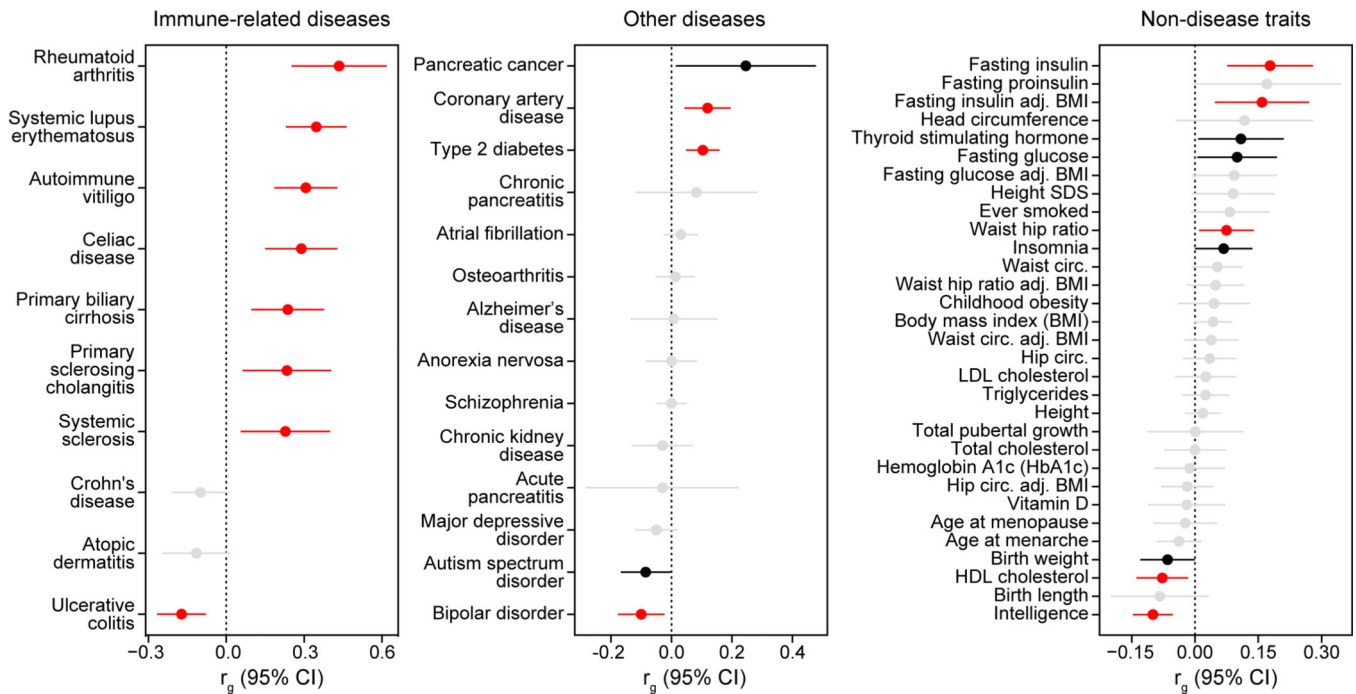
Extended Data



Extended Data Figure 1. Independent association signals at T1D risk loci.
 Bayes factors (natural log-transformed) for independent association signals at the known *PTPN2* locus (left) and the novel *BCL11A* locus (right). Variants are colored based on linkage disequilibrium (r^2) with the index variant for each signal.

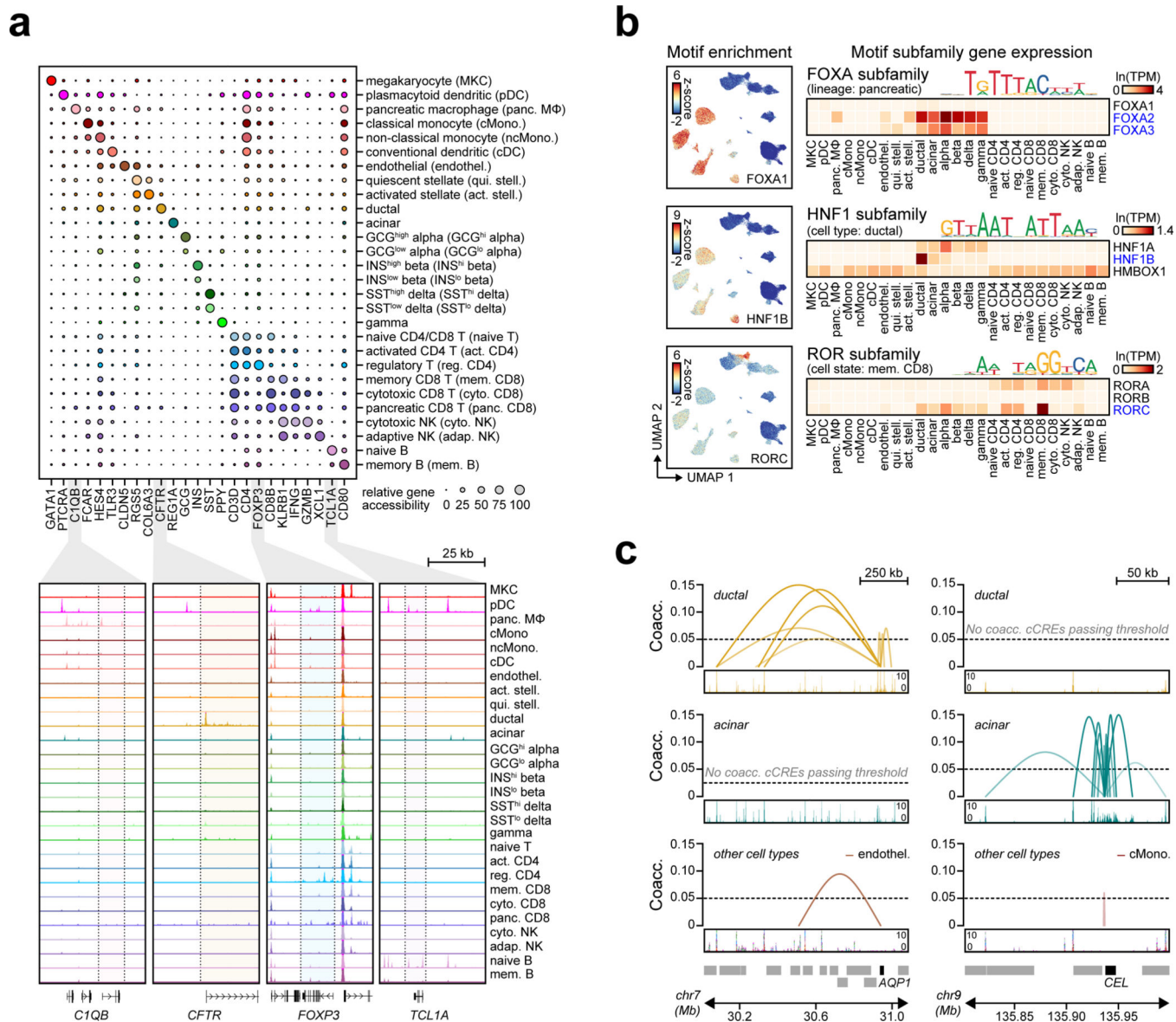
a**b****Extended Data Figure 2. Rare variants with large effects on T1D risk.**

(a) The relationship between minor allele frequency and T1D odds ratios (OR) for index variants at 136 T1D signals. Signals with common index variants and larger effect size estimates (PTPN22 1:114377568:A:G and INS 11:2182224:A:T) or rare index variants (MAF<0.005) are labeled. Points and lines represent estimates for OR and 95% CI. (b) Comparison of OR across cohorts for rare variants. Missing values indicate that the variant was not tested in the cohort. Points and lines represent estimates for OR and 95% CI.



Extended Data Figure 3. Genetic correlations between T1D and other traits.

Genetic correlations between T1D and immune-related diseases (left), other diseases (middle), and non-disease traits (right), adj.=adjusted, circ.=circumference. Two-sided p-values are adjusted for multiple comparisons with false discovery rate (FDR). Colors indicate significance: red – correlation is significant after FDR correction (FDR<0.1), black – correlation is nominally significant (p<0.05) but not significant after FDR correction, and grey – correlation is not significant. Points and lines represent genetic correlation estimates and 95% CI.

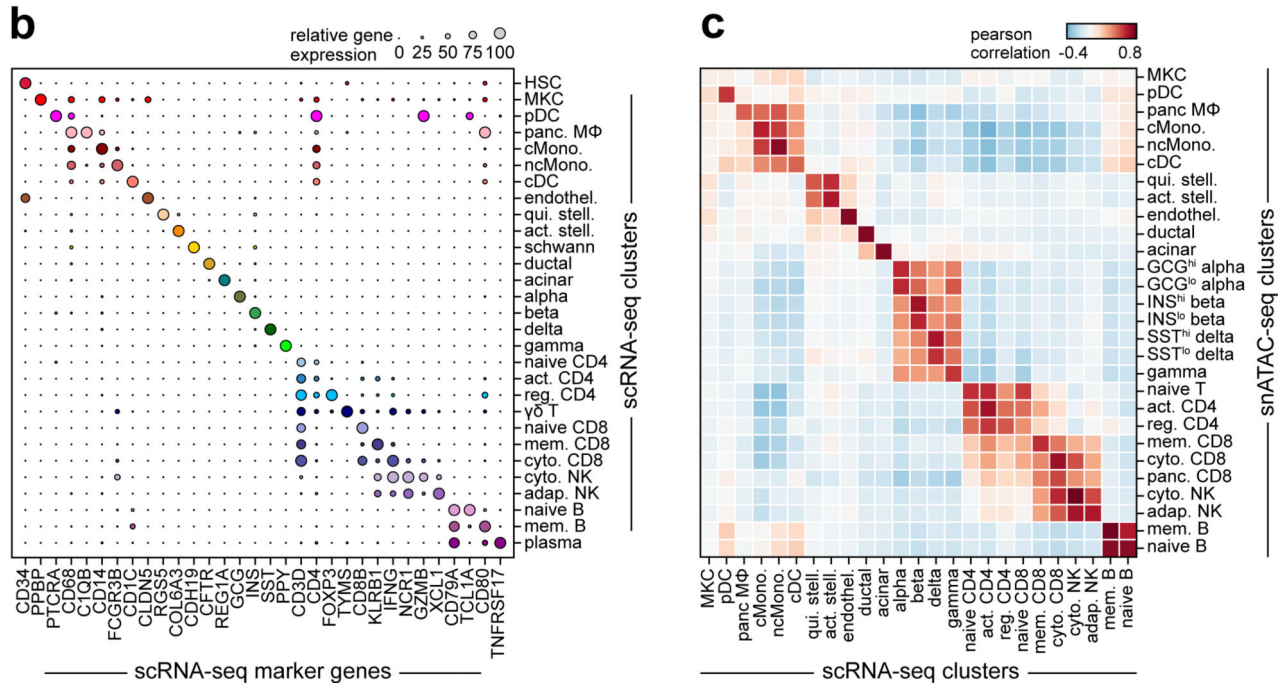
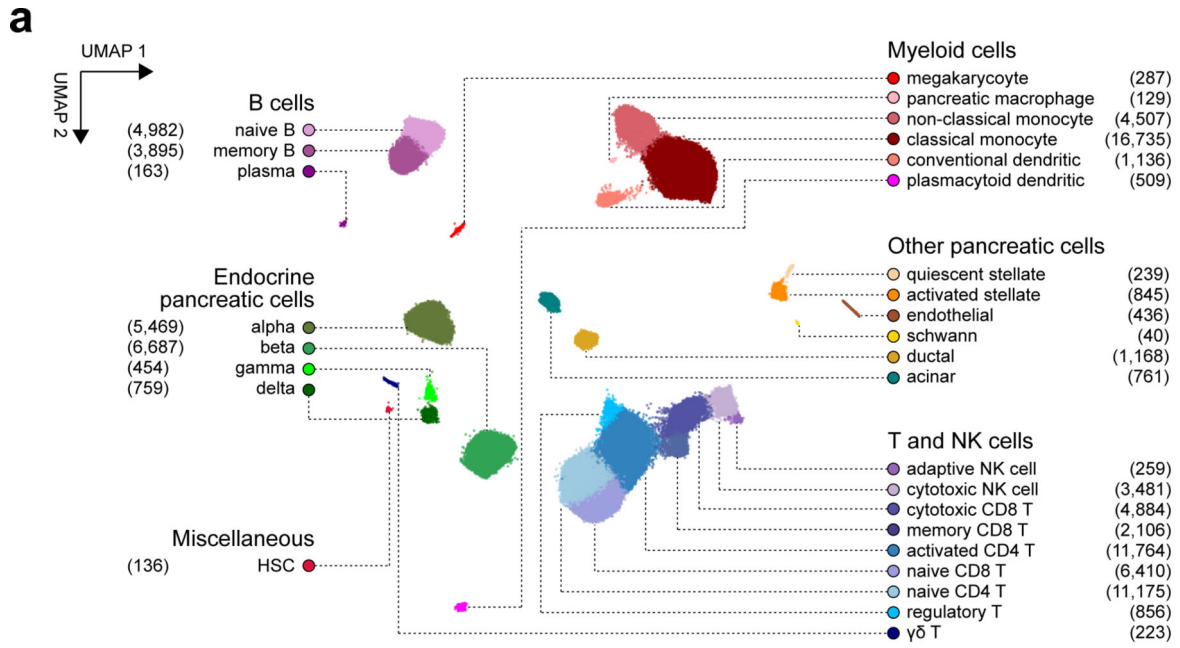


Extended Data Figure 4. Annotations derived from single cell chromatin accessibility of T1D-relevant tissues.

(a) Relative gene accessibility (column-normalized chromatin accessibility reads in gene bodies) showing examples of marker genes used to identify cluster labels. Aggregated chromatin accessibility profiles in a 50 kb window around selected marker genes (bottom).

(b) Single cell motif enrichment z-scores (left) and expression of motif subfamily members (right) for examples of TFs with lineage-, cell type-, or cell state-specific motif enrichment and expression. TFs with matching motif enrichment and expression are highlighted.

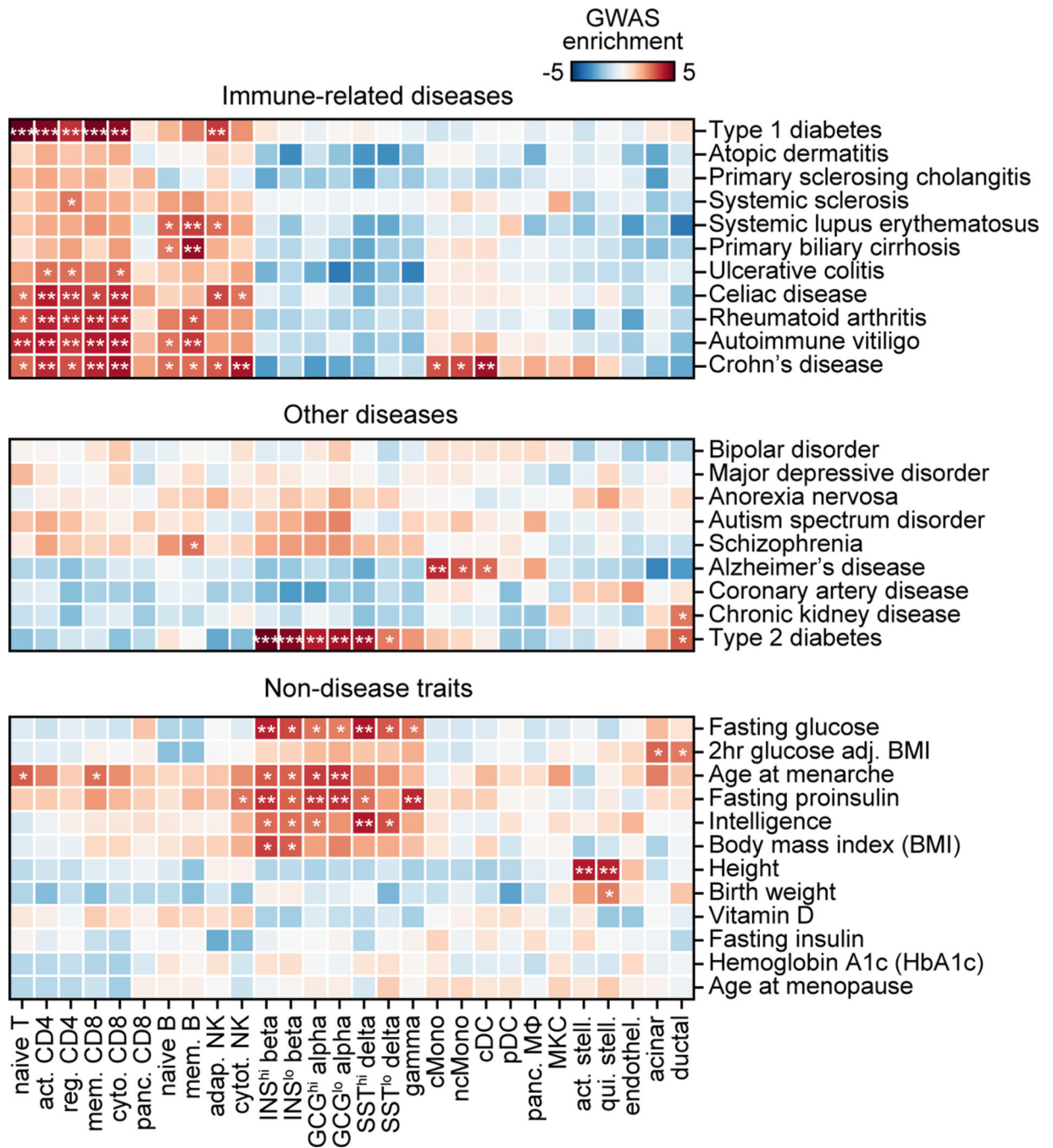
(c) Co-accessibility between *AQP1* and cCREs in ductal cells (left) and *CEL* and cCREs in acinar cells (right).



Extended Data Figure 5. Single cell RNA-seq reference map of PBMCs and pancreatic islets.

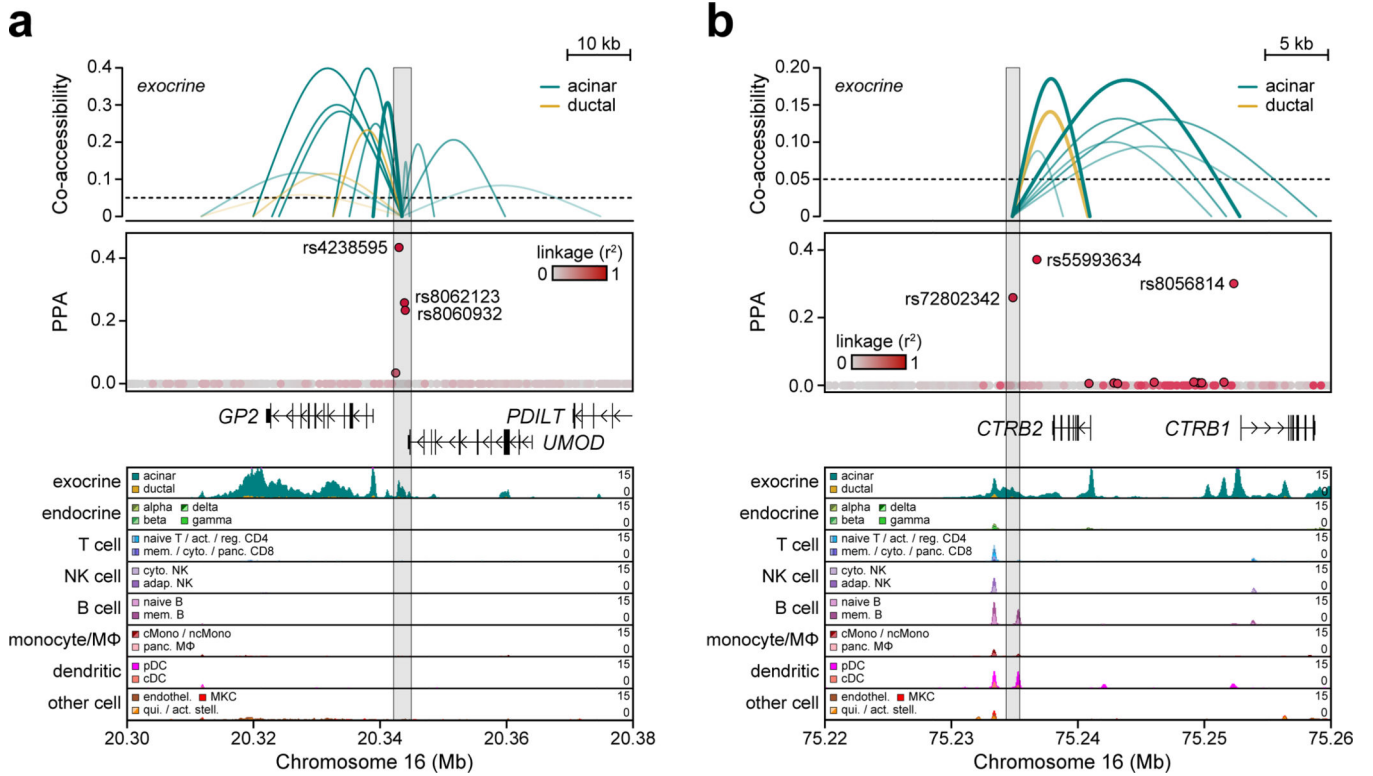
(a) Clustering of 90,495 expression profiles from single cell RNA-seq experiments of peripheral blood mononuclear cells and pancreatic islets from published studies. Cells are plotted on the first two UMAP components and colored based on cluster assignment. The number of cells in each cluster is shown next to its corresponding label. HSC, hematopoietic stem cell. $\gamma\delta$ T, gamma delta T. pDC, plasmacytoid dendritic. (b) Relative gene expression (average expression for all cells within a cluster and scaled from 0–100 across clusters) showing examples of marker genes used to assign cluster labels. (c) Pearson correlation

coefficient between gene expression and promoter accessibility specificity scores using a list containing the top 100 most specific genes for each scRNA-seq cluster found in snATAC-seq.



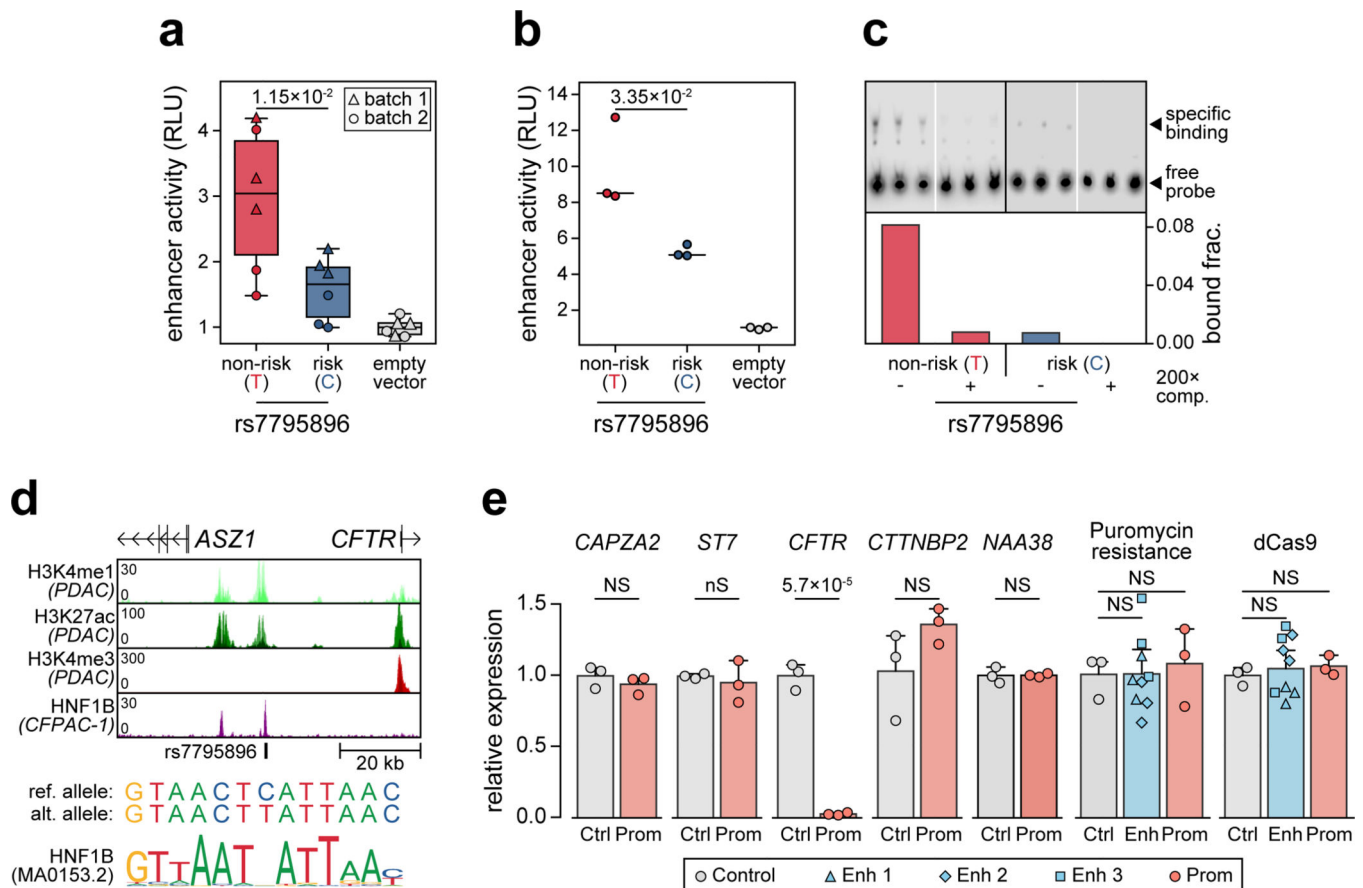
Extended Data Figure 6. GWAS enrichment for T1D compared to other diseases and traits Stratified LD score regression coefficient z-scores for autoimmune and inflammatory diseases (top), other diseases (middle), and non-disease quantitative endophenotypes (bottom) for cCREs active in immune and pancreatic cell types. Two sided p-values

were calculated from z-scores and multiple test correction was performed using FDR.
 ***FDR<0.001 **FDR<0.01 *FDR<0.1.



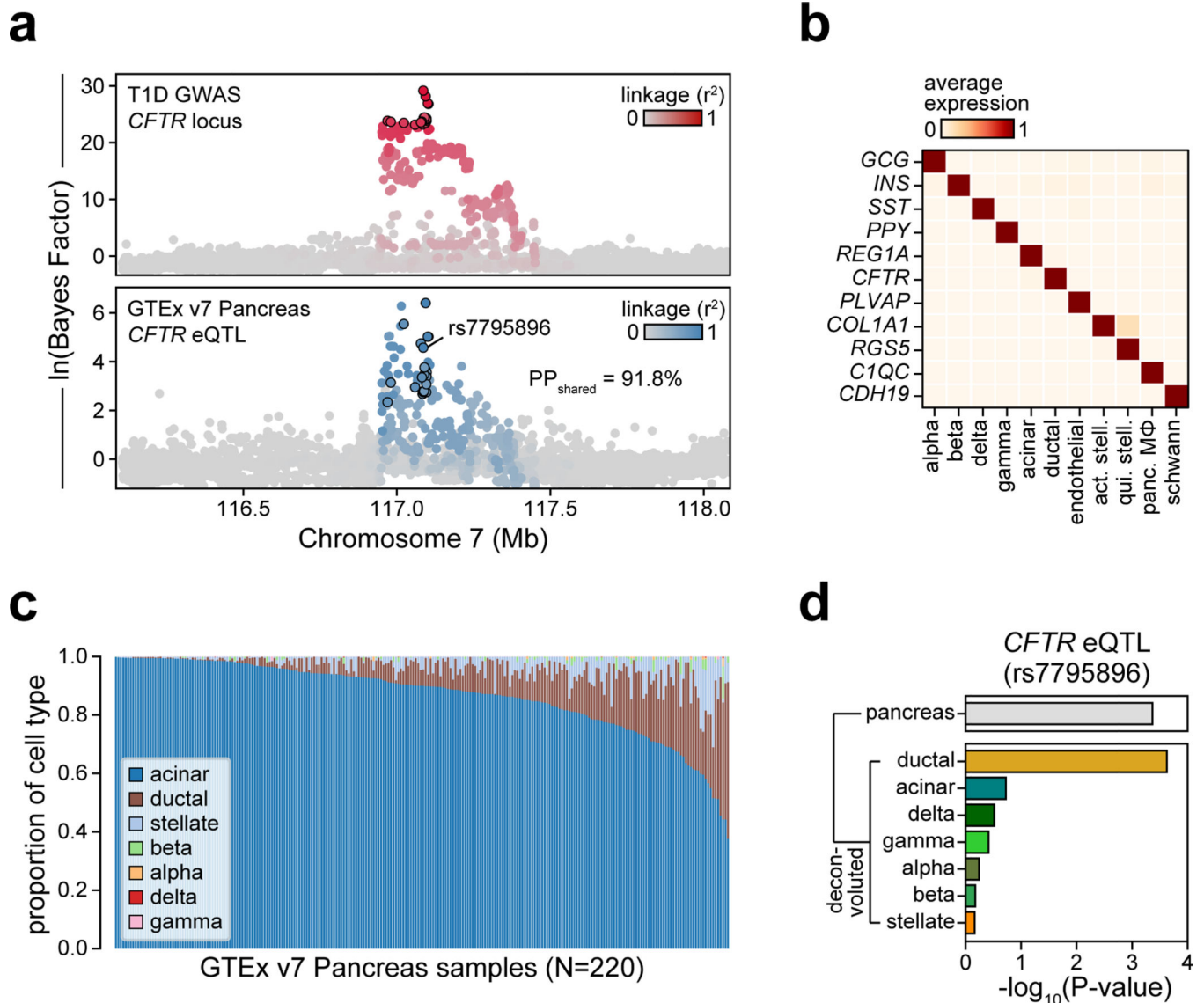
Extended Data Figure 7. Fine mapped variants linked to exocrine-specific genes

(a) The *GP2* locus contains three variants in a distal cCRE co-accessible with the *GP2* promoter in acinar cells which account for the majority of the causal probability (cPPA=0.98). Chromatin accessibility at both the distal cCRE and the *GP2* promoter is highly specific to acinar cells. (b) Variant rs72802342 at the *CTRB1/2/BCAR1* locus overlaps a distal cCRE co-accessible with the *CTRB2* and *CTRB1* promoters in acinar cells. Chromatin accessibility at the *CTRB1* and *CTRB2* promoters is highly specific to acinar cells. Variants contained in the 99% credible set are circled in black.

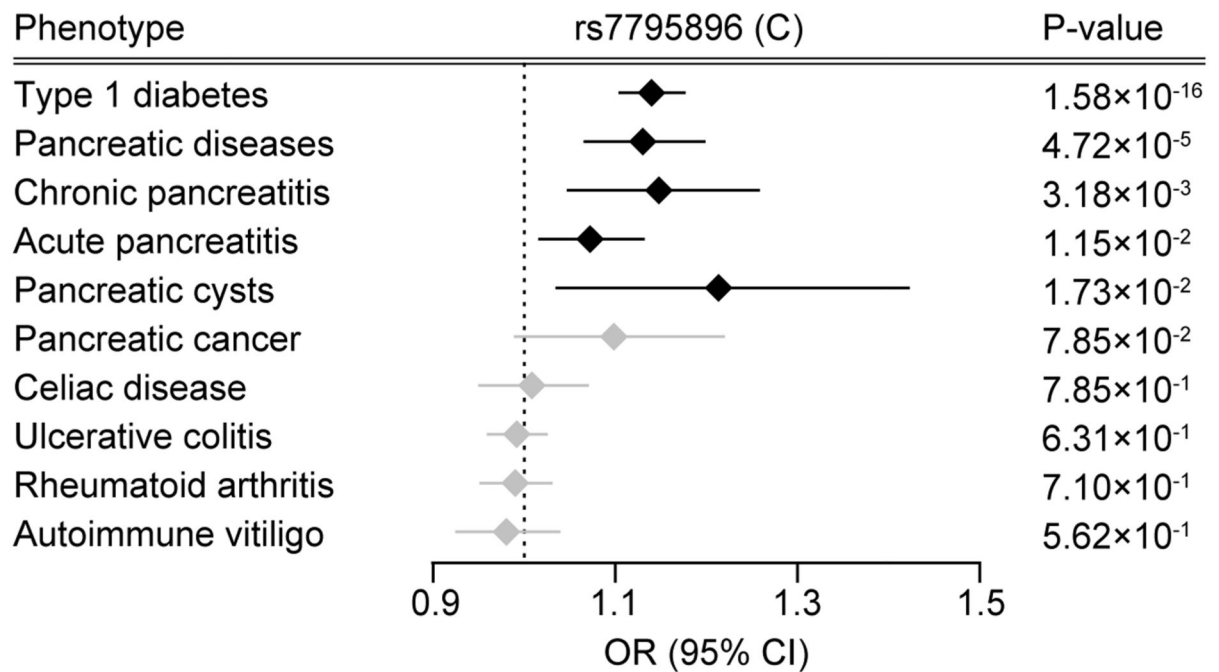
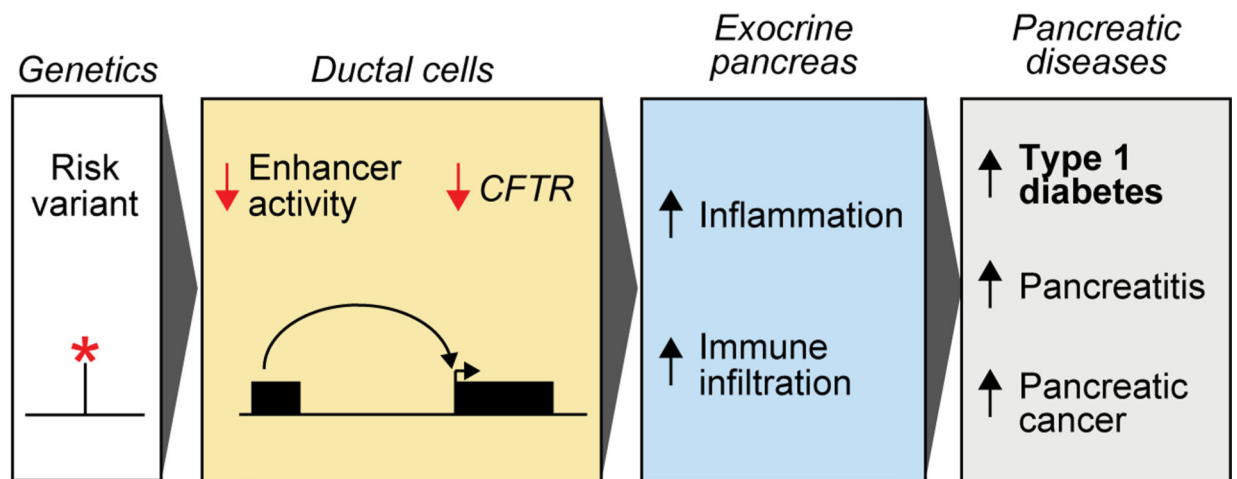


Extended Data Figure 8. rs7795896 has allelic effects on ductal enhancer activity.

(a) Relative luciferase units (RLU) for reporter containing 594 bp sequence surrounding rs7795896 in Capan 1 ($n=6$; 2 batches \times 3 transfections). Center line, median; box limits, 25th and 75th percentiles; whiskers extend to $1.5\times$ the IQR from the 25th and 75th percentiles. P-value by two-sided, two-way ANOVA. (b) Luciferase reporter assay in Capan-1 cells transfected with pGL4.23 minimal promoter plasmids containing rs7795896 in the forward orientation. Relative luciferase units (RLU) represent Firefly:Renilla ratios normalized to control cells transfected with the empty pGL4.23 vector. P-value by two-sided Student's t-test. (c) Electrophoretic mobility shift assay with nuclear extract from Capan-1 using probes for rs7795896 alleles, with or without 200 \times unlabeled competitor probe (200 \times comp.). Quantification of the bound fraction (specific binding / free probe). Data are from $n=1$ experiment. (d) rs7795896 overlaps histone marks of active enhancers (H3K4me1, H3K27ac; region: chr7:117,050,000–117,125,000, hg19) but not promoters (H3K4me3) in pancreatic ductal adenocarcinoma cell lines (PDAC: Capan-1, Capan-2, and CFPAC-1). rs7795896 overlaps a ChIP-seq peak for the transcription factor HNF1B in CFPAC-1 cells and a predicted HNF1B motif. (e) Relative expression for genes in a 2 Mb window around rs7795896 with non-zero expression and the puromycin resistance and dCas9 genes. Ctrl $n=3$ biological replicates; Enh $n=9$, 3 sgRNAs \times 3 biological replicates; Prom $n=3$ biological replicates. Data are mean \pm 95% CI. P-values by two-sided Student's t-test (Prom vs Ctrl) or two-sided ANOVA (Enh vs Ctrl); NS, not significant.



Extended Data Figure 9. rs7795896 affects *CFTR* expression levels in ductal cells. (a) Bayesian colocalization of T1D signal and *CFTR* pancreas eQTL. Variants in the T1D credible set are circled. (b) Expression of pancreatic cell type marker genes from scRNA-seq. (c) Proportions of selected pancreatic cell types estimated by MuSiC for 220 bulk pancreas RNA-seq samples from the GTEx v7 release using single cell expression profiles. (d) $-\log_{10}$ transformed two-sided uncorrected p-values from linear regression interaction between dosage and cell type proportion for the *CFTR* pancreas eQTL.

a**b****Extended Data Figure 10. Relationship between T1D and other pancreatic diseases.**

(a) rs7795896 GWAS association for T1D (from full meta-analysis), pancreatic disease, and autoimmune disease. Points and lines represent odds ratio estimates and 95% CI. Two-sided p-values from GWAS meta-analysis are unadjusted for multiple comparisons. (b) Variants regulating genes with specialized exocrine pancreas function influence T1D risk, and we hypothesize these effects are mediated through inflammation and immune infiltration.

Supplementary Material

Refer to Web version on PubMed Central for supplementary material.

ACKNOWLEDGEMENTS

This work was supported by NIH grants DK112155, DK120429 and DK122607 to K.J.G and M.S., and T32 GM008666 to R.G. We thank Samantha Kuan in the Ren Lab at the LICR for assistance with sequencing. Additional acknowledgements for each cohort are listed in the Supplementary Information.

DATA AVAILABILITY

Full summary statistics for the T1D GWAS have been deposited into the NHGRI-EBI GWAS catalog with accession number GCST90014023 and can be downloaded from http://ftp.ebi.ac.uk/pub/databases/gwas/summary_statistics/GCST90014001-GCST90015000/GCST90014023/. Sequencing data for snATAC-seq have been deposited into the NCBI Gene Expression Omnibus (GEO) with accession number GSE163160 and are available at <https://www.ncbi.nlm.nih.gov/geo/query/acc.cgi?acc=GSE163160>. Data obtained from the TFClass database are available at <http://tfclass.bioinf.med.uni-goettingen.de/> and from the PanglaoDB database at <https://panglaodb.se/>.

REFERENCES

1. Claussnitzer M. et al. A brief history of human disease genetics. *Nature* 577, 179–189 (2020). [PubMed: 31915397]
2. ENCODE Project Consortium. An integrated encyclopedia of DNA elements in the human genome. *Nature* 489, 57–74 (2012). [PubMed: 22955616]
3. Katsarou A. et al. Type 1 diabetes mellitus. *Nat. Rev. Dis. Primer* 3, 17016 (2017).
4. Onengut-Gumuscu S. et al. Fine mapping of type 1 diabetes susceptibility loci and evidence for colocalization of causal variants with lymphoid gene enhancers. *Nat. Genet* 47, 381–386 (2015). [PubMed: 25751624]
5. Barrett JC et al. Genome-wide association study and meta-analysis find that over 40 loci affect risk of type 1 diabetes. *Nat. Genet* 41, 703–707 (2009). [PubMed: 19430480]
6. Bradfield JP et al. A Genome-Wide Meta-Analysis of Six Type 1 Diabetes Cohorts Identifies Multiple Associated Loci. *PLOS Genet.* 7, e1002293 (2011).
7. Taliun D. et al. Sequencing of 53,831 diverse genomes from the NHLBI TOPMed Program. *bioRxiv* 563866 (2019) doi:10.1101/563866.
8. Aylward A, Chiou J, Okino M-L, Kadakia N. & Gaulton KJ Shared genetic risk contributes to type 1 and type 2 diabetes etiology. *Hum. Mol. Genet* (2018) doi:10.1093/hmg/ddy314.
9. Raeder H. et al. Mutations in the CEL VNTR cause a syndrome of diabetes and pancreatic exocrine dysfunction. *Nat. Genet* 38, 54–62 (2006). [PubMed: 16369531]
10. Ramos PS et al. A comprehensive analysis of shared loci between systemic lupus erythematosus (SLE) and sixteen autoimmune diseases reveals limited genetic overlap. *PLoS Genet.* 7, e1002406 (2011).
11. Gibson-Corley KN, Meyerholz DK & Engelhardt JF Pancreatic Pathophysiology in Cystic Fibrosis. *J. Pathol* 238, 311–320 (2016). [PubMed: 26365583]
12. Sharer N. et al. Mutations of the cystic fibrosis gene in patients with chronic pancreatitis. *N. Engl. J. Med* 339, 645–652 (1998). [PubMed: 9725921]
13. Diaferia GR et al. Dissection of transcriptional and cis-regulatory control of differentiation in human pancreatic cancer. *EMBO J.* 35, 595–617 (2016). [PubMed: 26769127]

14. Consortium GTEx et al. Genetic effects on gene expression across human tissues. *Nature* 550, 204–213 (2017). [PubMed: 29022597]
15. McWilliams RR et al. Cystic fibrosis transmembrane conductance regulator (CFTR) gene mutations and risk for pancreatic adenocarcinoma. *Cancer* 116, 203–209 (2010). [PubMed: 19885835]
16. Noone PG et al. Cystic fibrosis gene mutations and pancreatitis risk: relation to epithelial ion transport and trypsin inhibitor gene mutations. *Gastroenterology* 121, 1310–1319 (2001). [PubMed: 11729110]
17. Virostko J. et al. Pancreas Volume Declines During the First Year After Diagnosis of Type 1 Diabetes and Exhibits Altered Diffusion at Disease Onset. *Diabetes Care* 42, 248–257 (2019). [PubMed: 30552135]
18. Campbell-Thompson M, Rodriguez-Calvo T. & Battaglia M. Abnormalities of the Exocrine Pancreas in Type 1 Diabetes. *Curr. Diab. Rep* 15, 79 (2015). [PubMed: 26318606]
19. Camunas-Soler J. et al. Patch-Seq Links Single-Cell Transcriptomes to Human Islet Dysfunction in Diabetes. *Cell Metab.* 31, 1017–1031.e4 (2020). [PubMed: 32302527]
20. Fasolino M. et al. Multiomics single-cell analysis of human pancreatic islets reveals novel cellular states in health and type 1 diabetes. *bioRxiv* 2021.01.28.428598 (2021) doi:10.1101/2021.01.28.428598.
21. Hart NJ et al. Cystic fibrosis-related diabetes is caused by islet loss and inflammation. *JCI Insight* 3, (2018).
22. Valle A. et al. Reduction of circulating neutrophils precedes and accompanies type 1 diabetes. *Diabetes* 62, 2072–2077 (2013). [PubMed: 23349491]
23. Navis A. & Bagnat M. Loss of *cftr* function leads to pancreatic destruction in larval zebrafish. *Dev. Biol* 399, 237–248 (2015). [PubMed: 25592226]
24. Lin Y. et al. Genome-wide association meta-analysis identifies GP2 gene risk variants for pancreatic cancer. *Nat. Commun* 11, 3175 (2020). [PubMed: 32581250]
25. Wolpin BM et al. Genome-wide association study identifies multiple susceptibility loci for pancreatic cancer. *Nat. Genet* 46, 994–1000 (2014). [PubMed: 25086665]
26. Johansson BB et al. The role of the carboxyl ester lipase (CEL) gene in pancreatic disease. *Pancreatol. Off. J. Int. Assoc. Pancreatol. IAP AI* 18, 12–19 (2018).

ADDITIONAL REFERENCES

27. Purcell S. et al. PLINK: a tool set for whole-genome association and population-based linkage analyses. *Am. J. Hum. Genet* 81, 559–575 (2007). [PubMed: 17701901]
28. McCarthy S. et al. A reference panel of 64,976 haplotypes for genotype imputation. *Nat. Genet* 48, 1279–1283 (2016). [PubMed: 27548312]
29. 1000 Genomes Project Consortium et al. A global reference for human genetic variation. *Nature* 526, 68–74 (2015). [PubMed: 26432245]
30. Das S. et al. Next-generation genotype imputation service and methods. *Nat. Genet* 48, 1284–1287 (2016). [PubMed: 27571263]
31. Zhou W. et al. Efficiently controlling for case-control imbalance and sample relatedness in large-scale genetic association studies. *Nat. Genet* 50, 1335–1341 (2018). [PubMed: 30104761]
32. Bulik-Sullivan BK et al. LD Score regression distinguishes confounding from polygenicity in genome-wide association studies. *Nat. Genet* 47, 291–295 (2015). [PubMed: 25642630]
33. Evangelou M. et al. A method for gene-based pathway analysis using genomewide association study summary statistics reveals nine new type 1 diabetes associations. *Genet. Epidemiol* 38, 661–670 (2014). [PubMed: 25371288]
34. Benner C. et al. FINEMAP: efficient variable selection using summary data from genome-wide association studies. *Bioinforma. Oxf. Engl* 32, 1493–1501 (2016).
35. Bulik-Sullivan B. et al. An atlas of genetic correlations across human diseases and traits. *Nat. Genet* 47, 1236–1241 (2015). [PubMed: 26414676]

36. Ji S-G et al. Genome-wide association study of primary sclerosing cholangitis identifies new risk loci and quantifies the genetic relationship with inflammatory bowel disease. *Nat. Genet* 49, 269–273 (2017). [PubMed: 27992413]
37. Bentham J. et al. Genetic association analyses implicate aberrant regulation of innate and adaptive immunity genes in the pathogenesis of systemic lupus erythematosus. *Nat. Genet* 47, 1457–1464 (2015). [PubMed: 26502338]
38. Cordell HJ et al. International genome-wide meta-analysis identifies new primary biliary cirrhosis risk loci and targetable pathogenic pathways. *Nat. Commun* 6, 8019 (2015). [PubMed: 26394269]
39. Okada Y. et al. Genetics of rheumatoid arthritis contributes to biology and drug discovery. *Nature* 506, 376–381 (2014). [PubMed: 24390342]
40. de Lange KM et al. Genome-wide association study implicates immune activation of multiple integrin genes in inflammatory bowel disease. *Nat. Genet* 49, 256–261 (2017). [PubMed: 28067908]
41. Dubois PCA et al. Multiple common variants for celiac disease influencing immune gene expression. *Nat. Genet* 42, 295–302 (2010). [PubMed: 20190752]
42. Jin Y. et al. Genome-wide association studies of autoimmune vitiligo identify 23 new risk loci and highlight key pathways and regulatory variants. *Nat. Genet* 48, 1418–1424 (2016). [PubMed: 27723757]
43. Paternoster L. et al. Multi-ancestry genome-wide association study of 21,000 cases and 95,000 controls identifies new risk loci for atopic dermatitis. *Nat. Genet* 47, 1449–1456 (2015). [PubMed: 26482879]
44. López-Isac E. et al. GWAS for systemic sclerosis identifies multiple risk loci and highlights fibrotic and vasculopathy pathways. *Nat. Commun* 10, 4955 (2019). [PubMed: 31672989]
45. Jansen IE et al. Genome-wide meta-analysis identifies new loci and functional pathways influencing Alzheimer’s disease risk. *Nat. Genet* 51, 404–413 (2019). [PubMed: 30617256]
46. Mahajan A. et al. Fine-mapping type 2 diabetes loci to single-variant resolution using high-density imputation and islet-specific epigenome maps. *Nat. Genet* 50, 1505–1513 (2018). [PubMed: 30297969]
47. Nelson CP et al. Association analyses based on false discovery rate implicate new loci for coronary artery disease. *Nat. Genet* 49, 1385–1391 (2017). [PubMed: 28714975]
48. Stahl EA et al. Genome-wide association study identifies 30 loci associated with bipolar disorder. *Nat. Genet* 51, 793–803 (2019). [PubMed: 31043756]
49. Wray NR et al. Genome-wide association analyses identify 44 risk variants and refine the genetic architecture of major depression. *Nat. Genet* 50, 668–681 (2018). [PubMed: 29700475]
50. Grove J. et al. Identification of common genetic risk variants for autism spectrum disorder. *Nat. Genet* 51, 431–444 (2019). [PubMed: 30804558]
51. Watson HJ et al. Genome-wide association study identifies eight risk loci and implicates metabo-psychiatric origins for anorexia nervosa. *Nat. Genet* 51, 1207–1214 (2019). [PubMed: 31308545]
52. Schizophrenia Working Group of the Psychiatric Genomics Consortium. Biological insights from 108 schizophrenia-associated genetic loci. *Nature* 511, 421–427 (2014). [PubMed: 25056061]
53. Wuttke M. et al. A catalog of genetic loci associated with kidney function from analyses of a million individuals. *Nat. Genet* 51, 957–972 (2019). [PubMed: 31152163]
54. Nielsen JB et al. Biobank-driven genomic discovery yields new insight into atrial fibrillation biology. *Nat. Genet* 50, 1234–1239 (2018). [PubMed: 30061737]
55. Tachmazidou I. et al. Identification of new therapeutic targets for osteoarthritis through genome-wide analyses of UK Biobank data. *Nat. Genet* 51, 230–236 (2019). [PubMed: 30664745]
56. Wheeler E. et al. Impact of common genetic determinants of Hemoglobin A1c on type 2 diabetes risk and diagnosis in ancestrally diverse populations: A transethnic genome-wide meta-analysis. *PLoS Med.* 14, e1002383 (2017).
57. Horikoshi M. et al. Genome-wide associations for birth weight and correlations with adult disease. *Nature* 538, 248–252 (2016). [PubMed: 27680694]

58. Yengo L. et al. Meta-analysis of genome-wide association studies for height and body mass index in ~700000 individuals of European ancestry. *Hum. Mol. Genet* 27, 3641–3649 (2018). [PubMed: 30124842]
59. Jiang X. et al. Genome-wide association study in 79,366 European-ancestry individuals informs the genetic architecture of 25-hydroxyvitamin D levels. *Nat. Commun* 9, 260 (2018). [PubMed: 29343764]
60. Manning AK et al. A genome-wide approach accounting for body mass index identifies genetic variants influencing fasting glycaemic traits and insulin resistance. *Nat. Genet* 44, 659–669 (2012). [PubMed: 22581228]
61. Day FR et al. Large-scale genomic analyses link reproductive aging to hypothalamic signaling, breast cancer susceptibility and BRCA1-mediated DNA repair. *Nat. Genet* 47, 1294–1303 (2015). [PubMed: 26414677]
62. Day FR et al. Genomic analyses identify hundreds of variants associated with age at menarche and support a role for puberty timing in cancer risk. *Nat. Genet* 49, 834–841 (2017). [PubMed: 28436984]
63. Savage JE et al. Genome-wide association meta-analysis in 269,867 individuals identifies new genetic and functional links to intelligence. *Nat. Genet* 50, 912–919 (2018). [PubMed: 29942086]
64. Strawbridge RJ et al. Genome-wide association identifies nine common variants associated with fasting proinsulin levels and provides new insights into the pathophysiology of type 2 diabetes. *Diabetes* 60, 2624–2634 (2011). [PubMed: 21873549]
65. Saxena R. et al. Genetic variation in GIPR influences the glucose and insulin responses to an oral glucose challenge. *Nat. Genet* 42, 142–148 (2010). [PubMed: 20081857]
66. Tobacco and Genetics Consortium. Genome-wide meta-analyses identify multiple loci associated with smoking behavior. *Nat. Genet* 42, 441–447 (2010). [PubMed: 20418890]
67. Shungin D. et al. New genetic loci link adipose and insulin biology to body fat distribution. *Nature* 518, 187–196 (2015). [PubMed: 25673412]
68. Cousminer DL et al. Genome-wide association and longitudinal analyses reveal genetic loci linking pubertal height growth, pubertal timing and childhood adiposity. *Hum. Mol. Genet* 22, 2735–2747 (2013). [PubMed: 23449627]
69. Taal HR et al. Common variants at 12q15 and 12q24 are associated with infant head circumference. *Nat. Genet* 44, 532–538 (2012). [PubMed: 22504419]
70. Teumer A. et al. Genome-wide analyses identify a role for SLC17A4 and AADAT in thyroid hormone regulation. *Nat. Commun* 9, (2018).
71. Jansen PR et al. Genome-wide analysis of insomnia in 1,331,010 individuals identifies new risk loci and functional pathways. *Nat. Genet* 51, 394–403 (2019). [PubMed: 30804565]
72. van der Valk RJP et al. A novel common variant in DCST2 is associated with length in early life and height in adulthood. *Hum. Mol. Genet* 24, 1155–1168 (2015). [PubMed: 25281659]
73. Willer CJ et al. Discovery and refinement of loci associated with lipid levels. *Nat. Genet* 45, 1274–1283 (2013). [PubMed: 24097068]
74. Felix JF et al. Genome-wide association analysis identifies three new susceptibility loci for childhood body mass index. *Hum. Mol. Genet* 25, 389–403 (2016). [PubMed: 26604143]
75. Chiou J. et al. Single cell chromatin accessibility reveals pancreatic islet cell type- and state-specific regulatory programs of diabetes risk. *bioRxiv* 693671 (2019) doi:10.1101/693671.
76. Preissl S. et al. Single-nucleus analysis of accessible chromatin in developing mouse forebrain reveals cell-type-specific transcriptional regulation. *Nat. Neurosci* 21, 432–439 (2018). [PubMed: 29434377]
77. Cusanovich DA et al. Multiplex Single Cell Profiling of Chromatin Accessibility by Combinatorial Cellular Indexing. *Science* 348, 910–914 (2015). [PubMed: 25953818]
78. Li H. & Durbin R. Fast and accurate long-read alignment with Burrows-Wheeler transform. *Bioinforma. Oxf. Engl* 26, 589–595 (2010).
79. Li H. et al. The Sequence Alignment/Map format and SAMtools. *Bioinforma. Oxf. Engl* 25, 2078–2079 (2009).

80. Wolf FA, Angerer P. & Theis FJ SCANPY: large-scale single-cell gene expression data analysis. *Genome Biol.* 19, 15 (2018). [PubMed: 29409532]
81. Korsunsky I. et al. Fast, sensitive and accurate integration of single-cell data with Harmony. *Nat. Methods* 16, 1289–1296 (2019). [PubMed: 31740819]
82. Traag VA, Waltman L. & van Eck NJ From Louvain to Leiden: guaranteeing well-connected communities. *Sci. Rep* 9, 1–12 (2019). [PubMed: 30626917]
83. Franzén O, Gan L-M & Björkegren JLM PanglaoDB: a web server for exploration of mouse and human single-cell RNA sequencing data. *Database J. Biol. Databases Curation* 2019, (2019).
84. Xin Y. et al. Pseudotime Ordering of Single Human β -Cells Reveals States of Insulin Production and Unfolded Protein Response. *Diabetes db180365* (2018) doi:10.2337/db18-0365.
85. Zhang Y. et al. Model-based analysis of ChIP-Seq (MACS). *Genome Biol.* 9, R137 (2008). [PubMed: 18798982]
86. Amemiya HM, Kundaje A. & Boyle AP The ENCODE Blacklist: Identification of Problematic Regions of the Genome. *Sci. Rep* 9, 1–5 (2019). [PubMed: 30626917]
87. Quinlan AR & Hall IM BEDTools: a flexible suite of utilities for comparing genomic features. *Bioinformatics* 26, 841–842 (2010). [PubMed: 20110278]
88. Arda HE et al. A Chromatin Basis for Cell Lineage and Disease Risk in the Human Pancreas. *Cell Syst.* 7, 310–322.e4 (2018). [PubMed: 30145115]
89. Calderon D. et al. Landscape of stimulation-responsive chromatin across diverse human immune cells. *Nat. Genet* 51, 1494–1505 (2019). [PubMed: 31570894]
90. McLean CY et al. GREAT improves functional interpretation of cis-regulatory regions. *Nat. Biotechnol* 28, 495–501 (2010). [PubMed: 20436461]
91. Schep AN, Wu B, Buenrostro JD & Greenleaf WJ chromVAR: inferring transcription-factor-associated accessibility from single-cell epigenomic data. *Nat. Methods* 14, 975–978 (2017). [PubMed: 28825706]
92. Khan A. et al. JASPAR 2018: update of the open-access database of transcription factor binding profiles and its web framework. *Nucleic Acids Res.* 46, D1284 (2018). [PubMed: 29161433]
93. Wingender E, Schoeps T, Haubrock M. & Dönitz J. TFClass: a classification of human transcription factors and their rodent orthologs. *Nucleic Acids Res.* 43, D97–102 (2015). [PubMed: 25361979]
94. Pliner HA et al. Cicero Predicts cis-Regulatory DNA Interactions from Single-Cell Chromatin Accessibility Data. *Mol. Cell* 71, 858–871.e8 (2018). [PubMed: 30078726]
95. Harrow J. et al. GENCODE: the reference human genome annotation for The ENCODE Project. *Genome Res.* 22, 1760–1774 (2012). [PubMed: 22955987]
96. Finucane HK et al. Partitioning heritability by functional annotation using genome-wide association summary statistics. *Nat. Genet* 47, 1228–1235 (2015). [PubMed: 26414678]
97. Cusanovich DA et al. A Single-Cell Atlas of In Vivo Mammalian Chromatin Accessibility. *Cell* 174, 1309–1324.e18 (2018). [PubMed: 30078704]
98. Wakefield J. Bayes factors for genome-wide association studies: comparison with P-values. *Genet. Epidemiol* 33, 79–86 (2009). [PubMed: 18642345]
99. Pickrell JK Joint analysis of functional genomic data and genome-wide association studies of 18 human traits. *Am. J. Hum. Genet* 94, 559–573 (2014). [PubMed: 24702953]
100. Namkung W. et al. Ca²⁺ activates cystic fibrosis transmembrane conductance regulator- and Cl⁻-dependent HCO₃⁻ transport in pancreatic duct cells. *J. Biol. Chem* 278, 200–207 (2003). [PubMed: 12409301]
101. Doench JG et al. Optimized sgRNA design to maximize activity and minimize off-target effects of CRISPR-Cas9. *Nat. Biotechnol* 34, 184–191 (2016). [PubMed: 26780180]
102. Hsu PD et al. DNA targeting specificity of RNA-guided Cas9 nucleases. *Nat. Biotechnol* 31, 827–832 (2013). [PubMed: 23873081]
103. Horlbeck MA et al. Compact and highly active next-generation libraries for CRISPR-mediated gene repression and activation. *eLife* 5, (2016).
104. Giambartolomei C. et al. Bayesian test for colocalisation between pairs of genetic association studies using summary statistics. *PLoS Genet.* 10, e1004383 (2014).

105. Hormozdiari F. et al. Colocalization of GWAS and eQTL Signals Detects Target Genes. *Am. J. Hum. Genet* 99, 1245–1260 (2016). [PubMed: 27866706]
106. Wang X, Park J, Susztak K, Zhang NR & Li M. Bulk tissue cell type deconvolution with multi-subject single-cell expression reference. *Nat. Commun* 10, 1–9 (2019). [PubMed: 30602773]

Author Manuscript

Author Manuscript

Author Manuscript

Author Manuscript

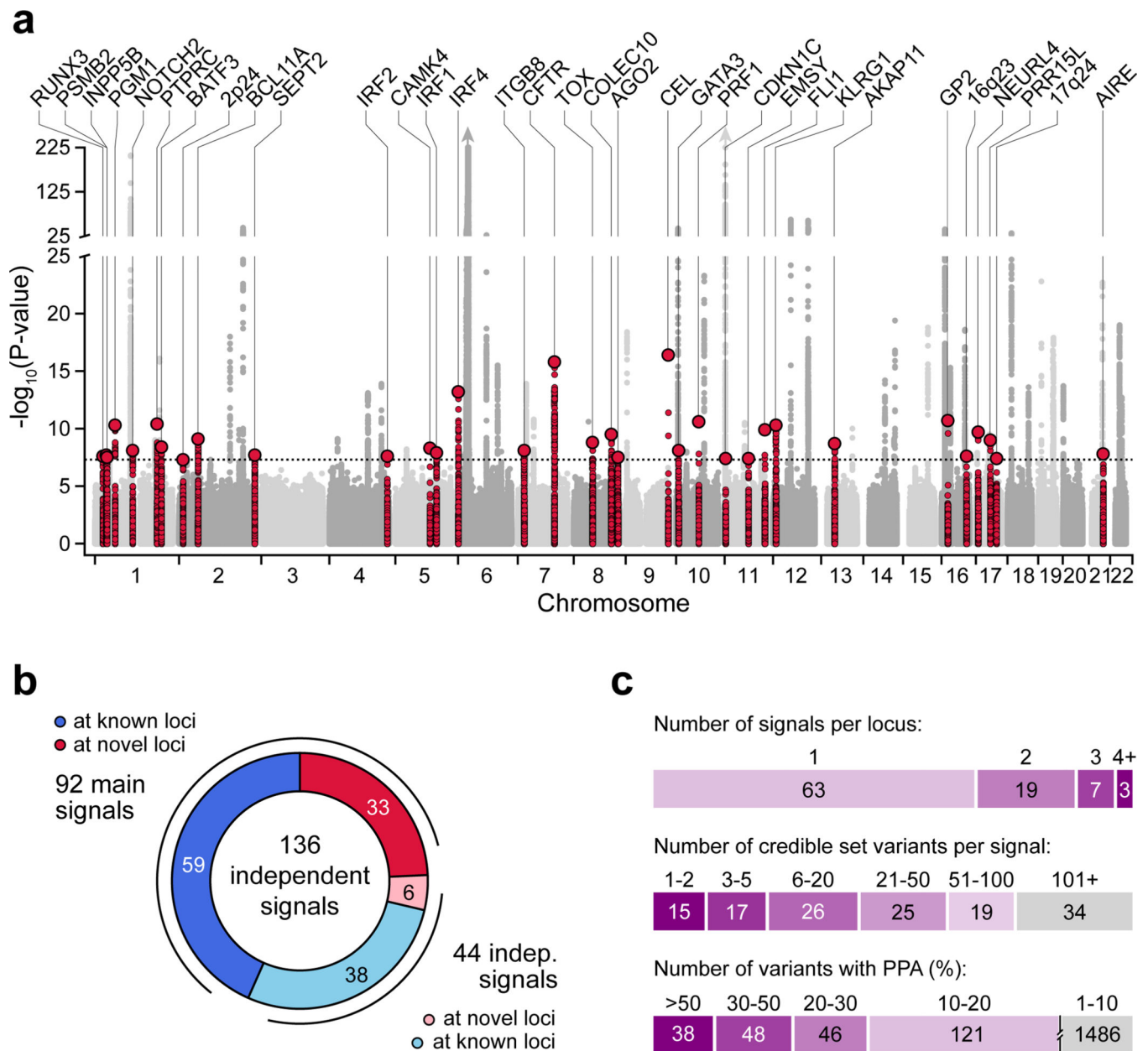


Figure 1. Genome-wide association and fine-mapping identifies novel T1D risk signals. (a) Genome-wide T1D association (two-sided $-\log_{10}$ transformed p-values from meta-analysis, unadjusted for multiple comparisons). Novel loci are colored (± 250 kb of the index variant) and labeled based on the nearest gene. Dotted line indicates genome-wide significance ($P=5 \times 10^{-8}$). (b) Breakdown of 136 T1D risk signals, including 92 main signals (59 known and 33 novel), and 44 independent signals (38 at known and 6 at novel loci). (c) Number of signals per locus (top), 99% credible set variants from fine-mapping (middle), and variants with posterior probability of association (PPA) at various thresholds (bottom).

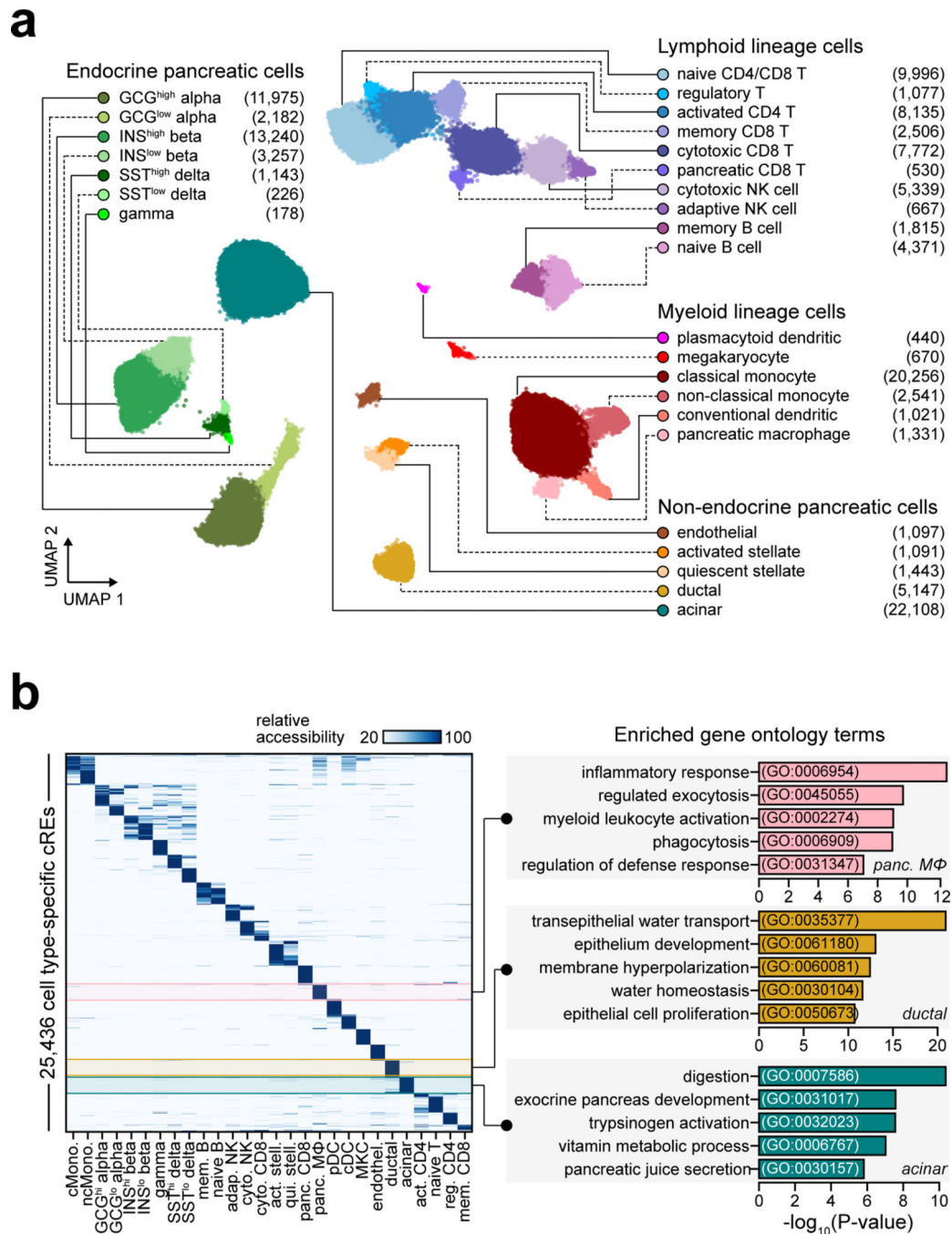


Figure 2. Reference map of single cell chromatin accessibility from T1D-relevant tissues. (a) Leiden clustering of single cell accessible chromatin profiles from 131,554 cells. Cells are plotted on the first two UMAP components, clusters are grouped into categories of cell types, and the number of cells per cluster are in parentheses. (b) Relative accessibility (row-normalized) for 25,436 cCREs most specific to each cluster (left), and enriched gene ontology terms for cCREs specific to pancreatic macrophages, ductal, and acinar cells (right).

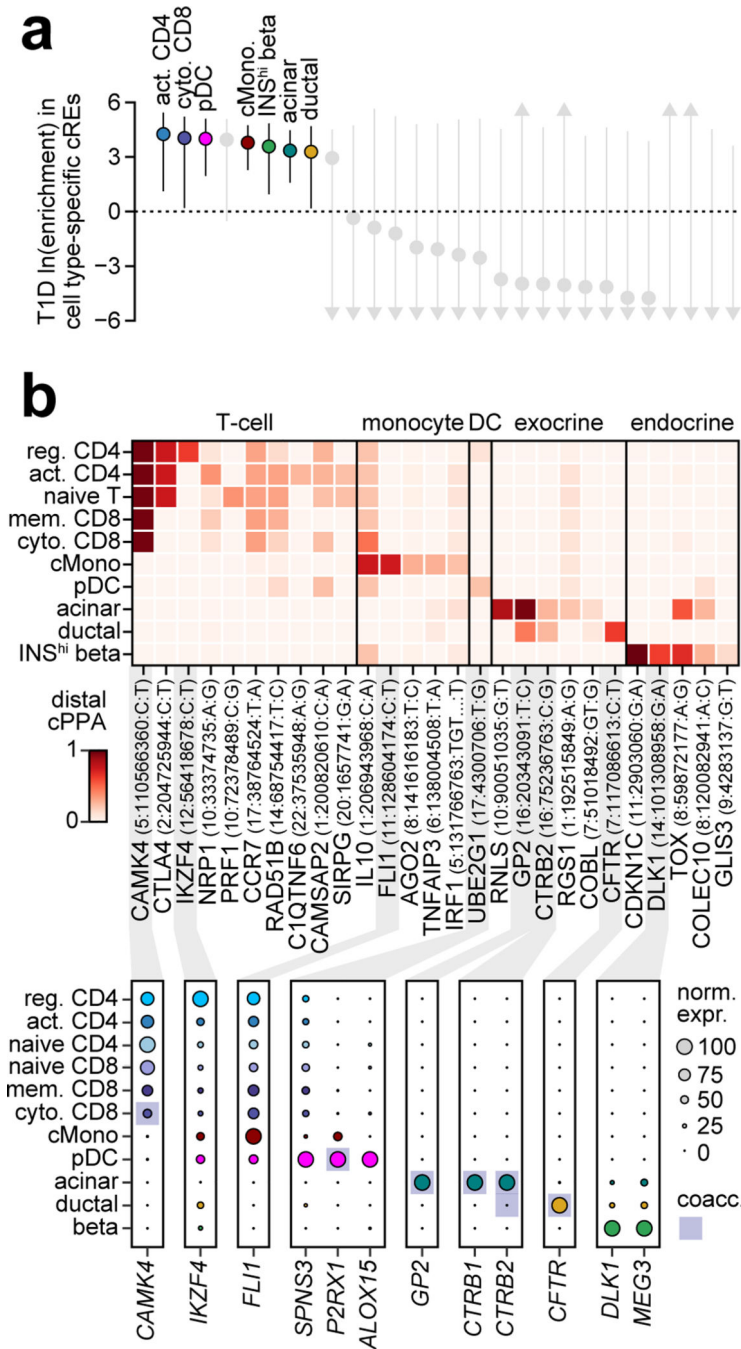


Figure 3. Cell type-specific enrichment and mechanisms of T1D risk variants.

(a) T1D enrichment within cell type-specific cCREs. Labeled cell types have positive enrichment and 95% CI lower bound >0. Data are natural log enrichment \pm 95% CI from fgwas. (b) T1D signals with highest cumulative PPA (cPPA) in cCREs for disease-enriched cell types (>0.20 cPPA for T cells and monocytes, >0.10 cPPA for other groups), and >0.01 cPPA away from the next closest group (top). Column-normalized expression for genes with TPM>1 in the highlighted cell type(s) and within \pm 500 kb of the index variant. Genes co-accessible with cCREs containing risk variants are annotated in rectangles (bottom).

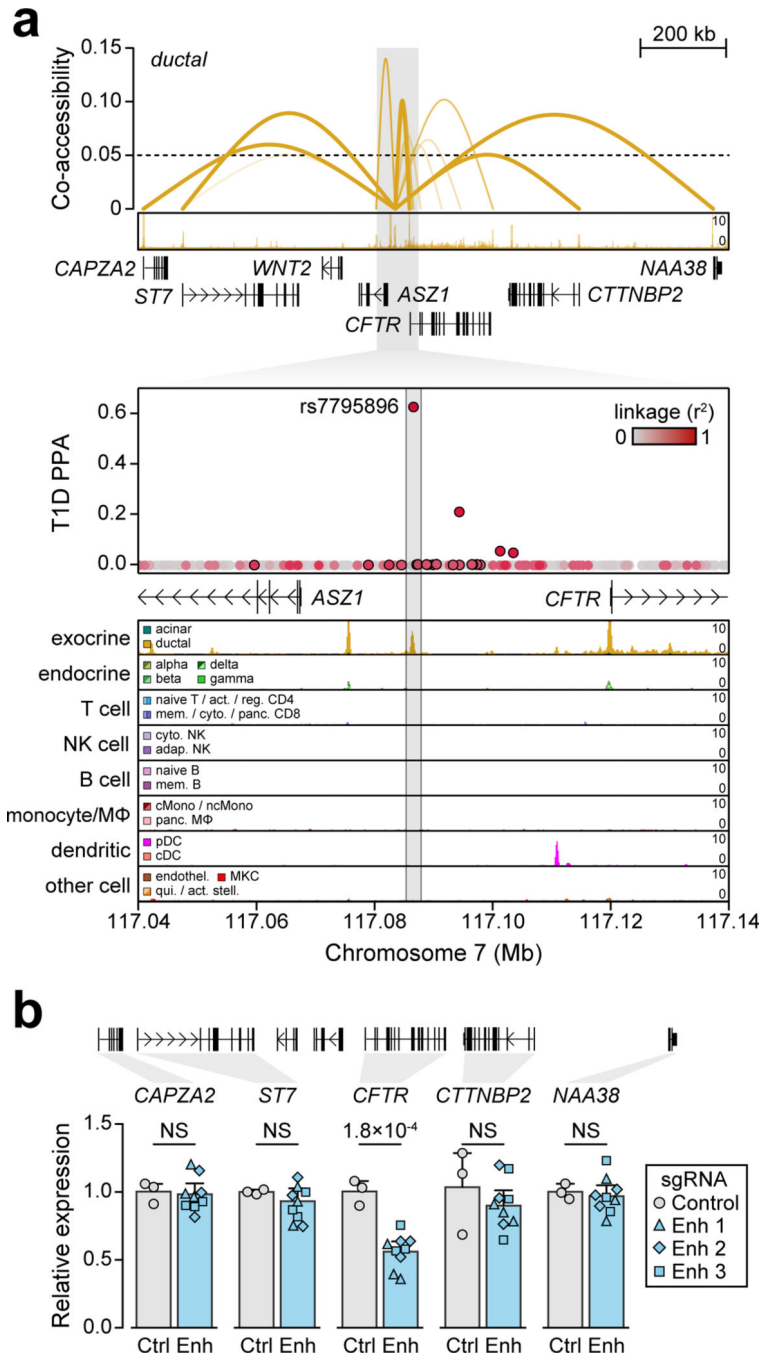


Figure 4. Fine-mapped T1D variant regulates *CFTR* in pancreatic ductal cells. (a) Variant rs7795896 at the *CFTR* locus mapped in a cCRE co-accessible with *CFTR* and other genes. Zoomed-in view shows the cCRE is ductal-specific. (b) Expression of genes co-accessible with the distal cCRE in CRISPR-inactivated enhancer (Enh; n=9, 3 sgRNAs × 3 biological replicates) compared to non-targeting control (Ctrl; n=3 biological replicates) in Capan-1. Data are mean ± 95% CI. P-values by two-sided ANOVA; NS, not significant.